Atmos. Chem. Phys., 23, 1285–1308, 2023
https://doi.org/10.5194/acp-23-1285-2023
© Author(s) 2023. This work is distributed under
the Creative Commons Attribution 4.0 License.

Atmospheric Chemistry and Physics
Open Access

Physicochemical properties of charcoal aerosols derived from biomass pyrolysis affect their ice-nucleating abilities at cirrus and mixed-phase cloud conditions

Fabian Mahrt[1,a], **Carolin Rösch**[1,b], **Kunfeng Gao**[1,2,3], **Christopher H. Dreimol**[4,5], **Maria A. Zawadowicz**[6], **and Zamin A. Kanji**[1]

[1]Department of Environmental System Sciences, Institute for Atmospheric and Climate Science, ETH Zurich, Zurich 8092, Switzerland
[2]School of Energy and Power Engineering, Beihang University, Beijing, China
[3]Shenyuan Honours College, Beihang University, Beijing, China
[4]Department of Civil, Environmental and Geomatic Engineering, Institute for Building Materials, ETH Zurich, 8093 Zurich, Switzerland
[5]Cellulose and Wood Materials Laboratory, Empa, 8600 Dübendorf, Switzerland
[6]Brookhaven National Laboratory, Environmental and Climate Sciences Department, Upton, New York, USA
[a]now at: Laboratory of Environmental Chemistry, Paul Scherrer Institute, 5232 Villigen, Switzerland
[b]now at: City of Zurich, Environmental and Health Protection Service – Air Quality, Zurich, Switzerland

Correspondence: Zamin A. Kanji (zamin.kanji@env.ethz.ch) and Fabian Mahrt (fabian.mahrt@psi.ch)

Received: 15 August 2022 – Discussion started: 22 August 2022
Revised: 22 December 2022 – Accepted: 27 December 2022 – Published: 24 January 2023

Abstract. Atmospheric aerosol particles play a key role in air pollution, health, and climate. Particles from biomass burning emissions are an important source of ambient aerosols, have increased over the past few decades, and are projected to further surge in the future as a result of climate and land use changes. Largely as a result of the variety of organic fuel materials and combustion types, particles emitted from biomass burning are often complex mixtures of inorganic and organic materials, with soot, ash, and charcoal having previously been identified as main particle types being emitted. Despite their importance for climate, their ice nucleation activities remain insufficiently understood, in particular for charcoal particles, whose ice nucleation activity has not been reported. Here, we present experiments of the ice nucleation activities of 400 nm size-selected charcoal particles, derived from the pyrolysis of two different biomass fuels, namely a grass charcoal and a wood charcoal. We find that the pyrolysis-derived charcoal types investigated do not contribute to ice formation via immersion freezing in mixed-phase cloud conditions. However, our results reveal considerable heterogeneous ice nucleation activity of both charcoal types at cirrus temperatures. An inspection of the ice nucleation results together with dynamic vapor sorption measurements indicates that cirrus ice formation proceeds via pore condensation and freezing. We find wood charcoal to be more ice-active than grass charcoal at cirrus temperatures. We attribute this to the enhanced porosity and water uptake capacity of the wood compared to the grass charcoal. In support of the results, we found a positive correlation of the ice nucleation activity of the wood charcoal particles and their chemical composition, specifically the presence of (inorganic) mineral components, based on single-particle mass spectrometry measurements. Even though correlational in nature, our results corroborate recent findings that ice-active minerals could largely govern the aerosol–cloud interactions of particles emitted from biomass burning emissions.

1 Introduction

Biomass burning emits greenhouse gases and aerosol particles into the atmosphere. The term "smoke" is generally used to describe all visible emissions of biomass burning, including gases and particulates (Cofer et al., 1997). The carbonaceous particulate matter associated with biomass burning smoke makes up a considerable fraction of the global aerosol burden (van der Werf et al., 2010; Schill et al., 2020; Reddy and Boucher, 2004; Andreae and Merlet, 2001). Such biomass burning aerosols are emitted from a wide range of processes, including wildfires, residential biomass combustion, and the industrial combustion of biofuels. As a result of global warming, deforestation, and changes in agricultural practices, the frequencies and intensities of biomass burning in the form of wildfires have increased over the past and are projected to further increase, enhancing the atmospheric burden of biomass-burning-derived particles (Ford et al., 2018; Moritz et al., 2012; Donovan et al., 2017; Westerling et al., 2006; Marlon et al., 2008; Holden et al., 2018). Thus, understanding the properties and environmental impacts of aerosol emitted from biomass burning is crucial. Owing to the complexity of the various emission sources that particulate matter from biomass burning encompasses, the aerosol types can display a range of different physical and chemical properties. Major particle types emitted into the atmosphere during biomass burning include soot, charcoal, and (fly) ash particles that are formed through different processes and at different stages of the combustion process (Chylek et al., 2015) and which are referred to as smoke particulates when considered to be a combined entity (Cofer et al., 1997). Sometimes, the latter can also contain soil particles lifted into the atmosphere in the case of strong wildfires (e.g., Wagner et al., 2018).

Soot particles form during the flaming stage of the combustion process in the presence of oxygen-containing air and at high temperatures, usually above 1000 °C, through the condensation of gas-phase intermediates (e.g., benzene, acetylene, and polycyclic aromatic hydrocarbons), i.e., by gas-to-particle conversion, leading to graphitic carbon spherules that cluster together into soot aggregates (Glassman et al., 2014). Characteristic for these soot particles is their fractal morphology, water insolubility, and microstructure, which contains a high refractory graphitic carbon content (Petzold et al., 2013). This graphitic carbon causes strong absorption of light in the near-visible spectral region due to the availability of non-localized electrons between the graphite layers. In contrast to soot, charcoal particles are formed from the pyrolysis of the biomass in the absence of, or limited access to, oxygen and during the smoldering stage of the combustion process. Compared to soot particles, charcoal forms at considerably lower temperatures, typically below ~ 600 °C. At these temperatures the (organic) fuel material decomposes, usually at limited air (oxygen) access, but the carbon does not vaporize, leading to incompletely oxidized pyrolysis products, including charcoal particles (Chylek et al., 2015; Andreae and Merlet, 2001). Thus, considering their origin, charcoal particles are primary aerosol particles, constituting charred, solid biomass material. Charcoal particles often retain the recognizable structure and morphology of their respective biomass fuel source (Sharma et al., 2004; Masiello, 2004). This makes their morphology more variable, with charcoal particles often having irregularly shaped, platy morphologies compared to the fractal-like morphology typically observed for soot aggregates. In addition, charcoal particles are generally characterized by higher elemental ratios of oxygen-to-carbon (O/C) and hydrogen-to-carbon (H/C; Hammes et al., 2007; Kim et al., 2003) compared to soot particles, i.e., a less graphitic microstructure, conferring a reduced absorbency (reduced sp2-bonded carbon content causes a lower absorption of radiation; Bond and Bergstrom, 2006) and reduced thermal and oxidative stability. Thus, overall, atmospheric charcoal and soot particles have different properties (e.g., Han et al., 2010). A large fraction of the charcoal resulting from wildfires remains on the Earth's surface. This sedimentary charcoal is often used in the context of reconstructing the characteristics of past fire and biomass burning (e.g., Adolf et al., 2018; Marlon et al., 2012). Yet, some entrainment by the wind erosion of post-burn areas can cause uplift and the atmospheric transport of surface charcoal particles, depending on their size and density (Clark, 1988). More often, the emission of charcoal particles into the atmosphere occurs as a result of buoyant thermal convection in strong wildfires that can result in considerable concentrations of charcoal particles and the long-range transport of these particles (Tinner et al., 2006; Clark, 1988).

Another important category of particles often formed during biomass burning is ash, which, in contrast to soot, contains only a limited amount of carbon. Ash denotes the solid, mineral-rich residuals remaining from combustion of organic substances, i.e., the refractory inorganic material. These noncombustible constituents often derive from mineral inclusions or heteroatoms (excluding carbon and hydrogen) in the biomass fuel material, such as, e.g., calcium (Ca), magnesium (Mg), and iron (Fe). While (bottom) ash describes the powdery material remaining on the ground of the burning site, the term "fine ash" (or sometimes "fly ash") is more commonly used in atmospheric science to describe the corresponding incombustible components that are emitted into the atmosphere with the burning emissions (Cofer et al., 1997). Fly ash particles are also emitted from coal combustion (e.g., Umo et al., 2015). While a previous study has estimated that only about 1 % of the total biomass burned results in airborne charcoal particles (Cofer et al., 1997), other work has suggested that up to 27 % of fire-derived carbon can result in charcoal particles (Zimmerman and Mitra, 2017). Nonetheless, an unambiguous discrimination and separation of the various particles types from biomass combustion is not always possible, and interdisciplinary accepted definitions are the matter of an ongoing debate (Andreae and Gelencser, 2006; Petzold et al., 2013; Cofer et al., 1997). In addition, open wildfires are dynamic processes in which the different flaming stages, i.e., stages of combustion processes and pyrolysis, are often present at the same time. Thus, the associated smoke plumes usually entrain combined emissions of the different particle types (i.e., smoke particulates). This is consistent with observations from smoke plumes, including organic and inorganic components (Maudlin et al., 2015; Vassilev et al., 2010, 2012; Posfai et al., 2003; Li et al., 2003; Adachi et al., 2022). Moreover, previous studies have also shown that biomass burning particles can contain crystalline mineral phases that form during the combustion process (Vassilev et al., 2013; Gao et al., 2014) and result from elements that are present within the fuel, including aluminum (Al), Ca, potassium (K), Fe, sodium (Na), and silicon (Si; Currie and Perry, 2007; Vassilev et al., 2010).

It is widely recognized that biomass burning particles have an important role in many environmental compartments. For instance, aerosol particles from biomass combustion affect the carbon cycle and biogeochemical processes when incorporated into surface reservoirs (e.g., Santín et al., 2016). Biomass-burning-derived particles also affect visibility and contribute to poor air quality, affecting human health (Reddington et al., 2015; Chen et al., 2017; Pardo et al., 2020). Yet, biomass burning particles also play a central role in atmospheric processes (Crutzen and Andreae, 1990; Andreae et al., 1994; Sokolik et al., 2019). For instance, they can affect the hydrological cycle and climate directly, through the absorption and scattering of light, and indirectly, when acting as cloud nuclei, affecting precipitation formation and cloud microphysical properties, with important ramifications for the regional and global energy budget (Bond et al., 2013; Bond and Bergstrom, 2006; Penner et al., 1992; Chylek and Wong, 1995; Koren et al., 2004; Kaufman and Koren, 2006; Kaufman and Fraser, 1997; Ditas et al., 2018; Yue et al., 2022). Despite the surge in the emissions of biomass burning particles and their importance for climate, their aerosol–cloud interactions, in particular their ability to act as ice-nucleating particles (INPs; Vali et al., 2015), remain associated with large uncertainties (Bond et al., 2013; Sokolik et al., 2019).

Several previous field and laboratory studies have reported the ice nucleation properties of particles derived from biomass burning for conditions relevant for cirrus or mixed-phase clouds (MPCs; Petters et al., 2009; Jahn et al., 2020; Jahl et al., 2021; Korhonen et al., 2020; Levin et al., 2016; McCluskey et al., 2014; Twohy et al., 2010; Chou et al., 2013; DeMott et al., 2009; Adams et al., 2020; Barry et al., 2021). For instance, DeMott et al. (2009) performed ice nucleation experiments at cirrus temperatures, i.e., $T < 235$ K, and found that ice formation on 100 nm diameter particles emitted from combustion of a range of fuel types, including rice straw, grass, and wood was, in most cases, indistinguishable from the homogeneous freezing of aqueous-solution droplets. Similarly, studies investigating the ice nucleation activity at mixed-phase cloud (MPC) conditions, i.e., $T > 235$ K and relative humidities with respect to water ($\mathrm{RH_w}$) greater than 100 %, have often found that particles emitted from biomass combustion have no or negligible heterogeneous immersion freezing activities within this temperature regime (e.g., Petters et al., 2009; Adams et al., 2020; Korhonen et al., 2020). Interestingly, biomass burning aerosols that formed ice via immersion freezing often contained inorganic material (McCluskey et al., 2014; Petters et al., 2009; Jahl et al., 2021; Jahn et al., 2020). For example, Petters et al. (2009) investigated the differences between the fuels that produced and did not produce INPs and observed that the fuel types producing INPs had, overall, a higher probability of containing K, nitrite ($\mathrm{NO_2^-}$), and inorganic material when compared to the fuels that did not show heterogeneous ice nucleation but only provided correlational evidence. Similarly, McCluskey et al. (2014) found that the INPs from two different wildfires were dominated by mineral or metal oxides, contributing 78 % and 67 %, respectively, to the total number of INPs analyzed per wildfire event (50–60 individual particles analyzed per event), with a high abundance of Ca and Al being characteristic features of these ice-active particles. Consistent with these observations, Jahn et al. (2020) recently attributed the immersion freezing activity to the inorganic components present within bottom ash particles produced during biomass burning and biomass burning aerosol particles sampled during the combustion of grass and wood fuels. Specifically, Jahn et al. (2020) found crystalline Ca- and Si-containing mineral phases that were both released and newly formed during the combustion process to largely govern the ice nucleation activity of these particles. Similarly, a positive correlation between the presence of $\mathrm{SiO_2}$ and Ca and the immersion freezing activity of ash particles has previously been reported (Grawe et al., 2016, 2018). The overall conclusions emerging from these studies is that inorganic mineral components are likely important for the ice nucleation activity of biomass burning particles. Nonetheless, due to the variety of different particle types emitted from biomass burning and the range of associated physicochemical properties, considerable uncertainty still exists regarding the ice nucleation activity of biomass burning particles. One particle type that is often emitted into the atmosphere during biomass burning, but whose ice nucleation activity has received little attention to date, is charcoal particles.

In this study, we investigate the ice nucleation ability of charcoal particles at temperatures relevant for both cirrus and MPC regimes in laboratory experiments. We studied submicron charcoal particles derived from the pyrolysis of two different types of biomasses, i.e., wood and grass fuel, in an attempt to cover different emission sources relevant for atmospheric charcoal particles. A suite of auxiliary measurements, including particle water uptake and loss, morphology, and chemical composition, complement our ice nucleation data in terms of characterizing the particle physicochemical properties and exploring potential links to their ice nucleation activity.

2 Materials and methods

2.1 Charcoal samples

Charcoal materials were obtained from the University of Zurich, Switzerland. The samples investigated are from two different biomass fuel types, including wood and grass charcoal. The wood charcoal was sourced from the debarked wood of chestnut trees (*Castanea sativa*), while the grass charcoal originated from rice straw (*Oryza sativa*). Charcoal particles from the chestnut trees were used as surrogates for aerosols emitted from the biomass burning of larger tree species. The *Castanea sativa* studied here is representative of forest growth across Europe, where it covers approximately 2.25×10^6 ha (Conedera et al., 2004). By contrast, charcoal particles from rice straw were used as surrogates for aerosols emitted from biomass burning in agricultural fields. Rice is one of the most important crops globally, and the burning of its straw is commonly practiced in many regions around the world to remove residues after harvest, or it is used as a low-cost fuel in heating stoves (Singh et al., 2021).

Both types of charcoal particles were produced by pyrolysis in a pure-nitrogen atmosphere at a temperature of 450 °C, using a commercial furnace (Carbolite Gero GmbH & Co. KG, Neuhausen, Germany; GERO GLO 11/40) operated at a nitrogen flow rate of $500\,\mathrm{L\,h^{-1}}$. Pyrolysis describes the thermochemical process in which the biomass is decomposed at elevated temperatures within an environment where oxygen is limited (Lehmann and Joseph, 2015). In contrast to pyrolysis, combustion describes the thermochemical process involving the reactions of the biomass with oxygen, where heat is released (Glassman et al., 2014). Biomass pyrolysis generally leads to the formation of a range of different compounds, including gaseous (volatile), liquid, and solid products, with the relative distribution of products being mainly dependent on the pyrolysis conditions (e.g., temperature and heating rate) and fuel material (Demirbas and Arin, 2002; Williams and Besler, 1996). Charcoal particles encompass the solid residue that is formed in a pyrolytic atmosphere. Any organic material associated with the biomass fuel that is volatile at the pyrolysis temperature was removed from the sample by the purge flow during the particle preparation. The charcoal particles investigated here represent typical low-temperature charcoals (Hammes et al., 2006). Details on the production method and a description of the physical and chemical properties is given elsewhere (Hammes et al., 2006, 2008). In brief, the O/C and H/C elemental ratios were found to be identical for wood charcoal and grass charcoal and were reported to be 0.3 and 0.7, respectively. In addition, both samples were dominated by aryl functionalities, i.e., aromatic carbon (70 %), as found by nuclear magnetic resonance spectroscopy, indicating the overall low abundance of hydrogen. The specific surface areas were found to be $2.0\,\mathrm{m^2\,g^{-1}} \pm 10\,\%$ and $5.9\,\mathrm{m^2\,g^{-1}} \pm 10\,\%$, for the wood and grass charcoal particles, respectively, as determined by nitrogen (N_2) adsorption, following the Brunauer–Emmett–Teller (BET) method (Brunauer et al., 1938). Hence, the surface areas of the charcoal particles investigated here are about an order of magnitude lower compared to other carbon-rich materials such as, e.g., soot (e.g., Ouf et al., 2019). We note that these specific surface area values are characteristic for low-temperature charcoals and that the properties of charcoal particles can strongly depend on the combustion conditions. For instance, the specific surface area of charcoal samples has been shown to increase with increasing maximum pyrolysis temperature, reaching values of several hundred square meters per gram of particle material for pyrolysis temperatures higher than those used here (Brown et al., 2006). In addition, the temperature of biomass burning in, e.g., real wildfires occurs over a range of different temperatures (e.g., Mondal and Sukumar, 2014). Thus, in the natural environment, biomass pyrolysis at different temperatures can result in charcoal particles with different physicochemical properties. As such, atmospheric charcoal particles can have different properties to the particles studied here.

For the ice nucleation experiments, the charcoal samples were aerosolized using a rotating brush aerosol generator (RBG; Palas GmbH, model 1000) and passed through a cyclone (URG Corporation; model URG-2000-30EHB; 50 % cutoff diameter ∼ 1 µm at a flow rate of $16.7\,\mathrm{L\,min^{-1}}$), in order to confine the aerosol size distribution to mostly submicron particles, before entering a $2.7\,\mathrm{m^3}$ stainless steel tank (Kanji et al., 2013). After filling the tank with charcoal aerosol up to a number concentration of approximately $4000–5000\,\mathrm{cm^{-3}}$, the particles were kept suspended with a continuously stirring fan mounted at the bottom of the tank. Particles for the ice nucleation experiments and for aerosol analysis were directly sampled from the tank, and a make-up flow of particle-free, high-purity nitrogen was used to keep the pressure in the tank constant throughout the experiment.

2.2 Ice nucleation measurements

Ice nucleation experiments were performed on size-selected aerosol particles at conditions relevant for both cirrus and MPCs. An aerosol stream sampled from the stainless-steel tank was passed through a differential mobility analyzer (DMA; TSI Incorporated, model 3080; polonium source aerosol-to-sheath flow ratio of 1 : 7) to select a quasi-monodisperse aerosol population with mobility diameters (d_m) of $d_\mathrm{m} = 400\,\mathrm{nm}$. The fraction of double-charged particles at the used flow conditions was approximately 15 % ($d_\mathrm{m} = 699\,\mathrm{nm}$, Wiedensohler, 1988).

2.2.1 HINC measurements (cirrus temperature regime)

Ice nucleation experiments in the cirrus temperature regime were performed using the horizontal ice nucleation chamber (HINC), which is described in detail elsewhere (Lacher et al., 2017). Briefly, in HINC, two ice-coated, horizontally oriented copper plates are separately cooled to different temperatures by individual recirculating coolers, achieving a temperature control along each of the continuous flow diffusion chamber (CFDC) walls of ± 0.1 K, corresponding to the thermocouple uncertainty. By setting the two walls of HINC to different sub-zero temperatures, a linear temperature gradient is established across the vertical extent of the ice chamber. This results in a nonlinear water vapor supersaturation profile across the vertical extent of the chamber, due to the nonlinear relation between temperature and saturation water vapor pressure, as described by the Clausius–Clapeyron equation (e.g., Lohmann et al., 2016). The aerosol particles are assumed to be mostly transported through the CFDC within the so-called aerosol lamina at the center of the chamber. The thickness (vertical extent) of the aerosol lamina is constrained by the ratio of a particle-free nitrogen sheath flow and the aerosol sample flow. For the experiments presented here, aerosol-to-sheath flow ratios between approximately 1 : 10 and 1 : 12 were used. The vertical extent of the aerosol lamina decreases with decreasing values for the aerosol-to-sheath flow ratio. The vertical extent of the aerosol lamina controls the portion of the supersaturation profile that can be experienced by the particles within HINC, i.e., it governs the variations in T and RH that the particles are exposed to. The RH conditions across the aerosol lamina at the center of the HINC chamber were calculated from the linear temperature profile between the two horizontal chamber walls, as per the parametrization given by Murphy and Koop (2005), and a maximum temperature uncertainty in either CFDC wall of 0.1 K, assuming a lower limit for the aerosol-to-sheath flow ratio of 1 : 10. This translates to an upper limit uncertainty in the relative humidity (RH), with respect to water ($\mathrm{RH_w}$) and with respect to ice ($\mathrm{RH_i}$), of approximately $\pm 3\,\%$ and $5\,\%$, respectively, at $T = 218$ K. At the same center temperature, and for a center $\mathrm{RH_w} = 105\,\%$, i.e., when the temperature gradient between the two walls is largest, the T variation across the aerosol lamina is approximately 1.1 K, again assuming an aerosol-to-sheath flow ratio of 1 : 10. These maximum RH and T uncertainties are conservative estimates and decrease for ice nucleation experiments at higher temperatures, as detailed elsewhere (e.g., Appendix D2 of Mahrt et al., 2018). The particle residence time (τ) within HINC can be varied by adjusting the position of a movable aerosol injector. Here, the position was fixed for all our experiments, corresponding to an average residence time of approximately 10 s for the temperature range investigated. Ice nucleation experiments in HINC were conducted as RH scans, where the RH is slowly increased ($<3\,\%\ \mathrm{RH_i}\ \mathrm{min}^{-1}$) at a fixed center temperature by increasing the temperature gradient between the two walls. The number of aerosol particles that act as INPs and form macroscopic ice crystal (n_{ice}) at a given RH are detected at the exit of HINC. By dividing n_{ice} by the total number concentration of aerosol particles entering HINC, n_{tot}, we calculate the activated fraction (AF) of charcoal particles given as follows:

$$\mathrm{AF} = \frac{n_{\mathrm{ice}}}{n_{\mathrm{tot}}}. \tag{1}$$

For all HINC experiments reported here, n_{ice} is given by the number of particles with diameters larger than 1 µm, as detected by an optical particle counter (OPC; model GT-526S; Met One Instruments, Inc., Grants Pass, OR, USA) at the exit of HINC. Given that the HINC experiments were all performed at $T \leq 233$ K, i.e., below the homogeneous ice nucleation temperature of pure water droplets, all particles considerably larger than that of the size-selected aerosols particles must be ice particles. Theoretical growth calculations that have assumed the pure diffusional growth of idealized spherical particles, using a conservative deposition coefficient of 0.1, suggest that ice particles grow to diameters beyond 1 µm within the residence time of HINC (~ 10 s) for a wide range of temperature and relative humidity conditions, as detailed in our earlier work (Mahrt et al., 2018). Given the similar temperature and relative humidity conditions used in our experiments herein, we expect the formation of sufficiently large ice particles to be detected by the OPC. Concurrently, the decrease in the ice particle size due to sublimation or melting during the transition from the exit of HINC to the OPC is assumed to be negligible, given the short transit time ($<10^{-4}$ s). The value of n_{tot} was determined by a condensation particle counter (CPC; TSI Incorporated; model 3776) operating in a low-flow mode ($0.3\ \mathrm{L\,min}^{-1}$), in parallel to HINC, and taking the dilution factor due to the aerosol-to-sheath flow into account. Uncertainty in the AF is 14 %, resulting from the propagated counting uncertainties of 10 % from each the OPC and the CPC. Each AF curve is corrected for background counts from, e.g., chamber internal frost particles, by measuring the AF for particle-filtered air at the start and target RH of each RH scan for a period of 5 min and linearly interpolating the background OPC counts for the RH range in between. All AF curves reported are averages of two to three independent RH scans. In HINC, ice nucleation experiments were performed at $218 \leq T \leq 233$ K, which are relevant temperatures for cirrus cloud formation.

2.2.2 IMCA-ZINC measurements (MPC temperature regime)

Immersion-freezing-mode experiments at $T > 230$ K were performed using a combination of the Zurich ice nucleation chamber (ZINC; Stetzer et al., 2008; Welti et al., 2009) and its vertical extension, the immersion mode cooling chamber (IMCA; Lüönd et al., 2010). The experimental setup has been described in detail previously (Lüönd et al., 2010; Welti et al., 2012). In short, the particles are first activated into cloud droplets in IMCA at $T = 313$ K. High supersaturation with respect to water of approximately 20 % at the top part of IMCA ensures cloud droplet activation of all particles, so that each aerosol particle becomes immersed into a single cloud droplet. As the particles flow through IMCA, the droplets, each with a single charcoal particle immersed, are continuously cooled to the experimental (aerosol lamina) temperature of ZINC, lowering the supersaturation to a value slightly above water saturation, in order to avoid the evaporation of the droplets upon reaching the supercooled regions of ZINC. In ZINC, a vertical CFDC with parallel-plate design, the droplets are exposed to freezing temperatures between approximately 230 and 255 K. Immersion freezing experiments were performed using so-called T scans, where the $\mathrm{RH_w}$ is fixed to value of 104 %, and the temperature is decreased in 2 K increments, from low to high values. At each temperature increment, the AF is used to determine the fraction of frozen droplets at the end of ZINC, which is given by the following:

$$\mathrm{AF}_{\text{IMCA-ZINC}} = \frac{n_{\text{ice}}}{n_{\text{ice}} + n_{\text{droplets}}}. \tag{2}$$

Here, n_{ice} and n_{droplets} define the number concentration of ice crystals and cloud droplets, respectively, formed within IMCA-ZINC and detected with an OPC (LIGHTHOUSE; Remote 5104) at the exit of the ZINC chamber. The uncertainty in AF results from a counting uncertainty of 10 % from both the OPC and the CPC, resulting in a 14 % relative error. The initial particle number concentration entering IMCA-ZINC was recorded by a CPC (TSI Incorporated; model 3787) operated in parallel. In the case of IMCA-ZINC experiments, n_{ice} denotes the number of particles with $d_{\mathrm{p}} > 2$ µm, as determined by the OPC. All AF curves are an average of three individual experimental runs and corrected for background counts determined from sampling particle-free air for a duration of 3 min at each temperature of the T scan. The temperature uncertainty in IMCA-ZINC measurements was ± 0.1 K, translating to a maximum uncertainty in $\mathrm{RH_w}$ ($\mathrm{RH_i}$) of approximately 3 % (5 %) at 218 K. The average particle residence time within ZINC was $\tau \approx 10$ s over the temperature range investigated here.

2.3 Auxiliary measurements for sample characterization

2.3.1 Transmission electron microscopy measurements

Aerosol particles from each sample were collected for transmission electron microscopy (TEM) analysis. Polydisperse aerosol particles were sampled from the stainless-steel tank and impacted on standard Cu-TEM grids with a continuous carbon film and 400 lines per inch mesh (Quantifoil Micro Tools GmbH, Großlöbichau, Germany). Particles were collected using the Zurich electron microscope impactor (ZEMI; Mahrt et al., 2018), a rotating drum impactor allowing for the individual control of the sample flow rate, sample time, and impaction distance. Collected particles were analyzed using a TEM JEOL JEM-1400 microscope (JEOL Ltd., Tokyo, Japan) equipped with a LaB6 (lanthanhexaborid) filament and operating at 120 kV.

2.3.2 Water vapor sorption measurements

Particle hygroscopicity was characterized by dynamic vapor sorption (DVS; Advantage ET 1; Surface Measurement Systems Ltd., London, UK). DVS gravimetrically measures the amount of water being taken up by the bulk sample by determining the relative mass change, Δm, between the sample under dry conditions ($\mathrm{RH_w} = 0$ %) and at each $\mathrm{RH_w}$ value during a DVS scan. The DVS instrument has a weighting precision of 0.1 µg, and the absolute uncertainty in $\mathrm{RH_w}$ amounts to ±0.5 %. The flow rate through the DVS was 200 mL $\mathrm{min^{-1}}$ of high purity $\mathrm{N_2}$ (5.0 grade) for our experiments, and the RH was controlled by humidifying the $\mathrm{N_2}$ flow with Milli-Q water . The bulk sample water uptake and loss were determined at 298 K by measuring the adsorption and desorption isotherms in 5 % and 3 % $\mathrm{RH_w}$ steps in the range of 0 %–80 % and 80 %–98 %, respectively. The value of Δm was determined at each $\mathrm{RH_w}$ step after quasi-equilibrium was reached, which was defined as a mass change rate below 0.0005 % $\mathrm{min^{-1}}$ over a period of 10 min. If this criterion was not met, then the mass that was reached after a maximum period of 1000 min at a given $\mathrm{RH_w}$ step was used instead to calculate the amount of water that was taken up during quasi-equilibrium. Prior to the DVS analysis, each sample was dried directly within the DVS sample chamber at a temperature of 298 K and over a period of 1000 min, in order to outgas any pre-adsorbed water, followed by a full sorption cycle, starting with the adsorption and subsequently the desorption measurements.

2.3.3 Chemical characterization

The chemical composition of the particles was analyzed using single-particle aerosol mass spectrometry. Specifically, we employed an aerosol time-of-flight mass spectrometer (ATOFMS; model 3800; TSI Incorporated) to obtain the chemical composition of individual aerosol particles as a function of the particle size. A detailed description of the ATOFMS can be found elsewhere (Gard et al., 1997; Noble and Prather, 1996; Prather et al., 1994). In brief, aerosols are sampled into the instrument through a critical orifice. Downstream of the orifice, an aerodynamic focusing lens (AFL), inertially focuses the particles, which exit the AFL through an acceleration nozzle, controlling the supersonic expansion of the particle loaded air and causing a size-dependent acceleration of the aerosols. Particle velocity is determined from light-scattering pulses by measuring the transit time between two diode-pumped, solid-state continuous wave laser beams operating at a wavelength of $\lambda = 405$ nm (Livermore Instruments Inc., model FMXL405). The vacuum aerodynamic particle diameter, d_{va}, is calculated from the measured velocity using a calibration curve obtained when using polystyrene latex spheres of known size and density. In the mass spectrometry source region, a pulsed ultraviolet neodymium-doped yttrium aluminum garnet (Nd:YAG) laser (Big Sky Laser Technologies Inc., now trading as Quantel USA; Ultra Series 230), with a wavelength of $\lambda = 266$ nm is used to ionize the particles. The ATOFMS employs a laser ablation ionization technique, which allows the detection of refractory aerosol components within the charcoal particles. The beam diameter of the Nd:YAG laser used was ~ 2.4 mm, and the energy of the pulse can be varied, enabling some control over the fragmentation of the analyte. Here, a typical pulse energy of about 1 mJ was used in order to allow for a more complete ionization of the particles. Positive and negative ions are detected simultaneously, using a dual-reflectron time-of-flight mass spectrometer.

The mass calibration of the time-of-flight signal was obtained from analyzing the particles of a known chemical composition prior to the experiments. Single-particle mass spectra from the ATOFMS were imported into the TSI firmware MS Analyze, where basic analysis, i.e., mass and size calibrations were applied to the data sets. For the evaluation of the single-particle mass spectral data, the calibrated data sets were then imported and processed within the flexible analysis toolkit for the exploration of single-particle mass spectrometer data (FATES; Sultana et al., 2017a). FATES includes different features for ATOFMS data postprocessing, such as sorting the mass into groups, or converting the mass spectra into spectra with unit mass resolution (i.e., stick spectra), which is achieved by integrating the ion signal peak width around integer mass-to-charge (m/z) values or calculating the average spectra for a given set of single-particle spectra. Here, we report the average mass spectra in terms of relative peak area and focus on the analysis of the averaged stick spectra of each charcoal type, examining these with respect to the presence of marker peaks. We note that different ions can result in the same m/z ratio, and here a peak assignment is informed by a comparison with the literature data, where different particles types of a known composition with instruments that use a $\lambda = 266$ nm Nd:YAG laser for aerosol particle ablation and ionization, including other (commercial) ATOFMS instruments and, for example, the ALABAMA and the SPASS mass spectrometers (Brands et al., 2011; Erdmann et al., 2005). The particle analysis by the ATOFMS was achieved by directly sampling from the stainless-steel aerosol tank, which is similar to the ice nucleation measurements but using polydisperse aerosol. The objective of our ATOFMS analysis was to gain information on the average chemical composition of the two charcoal types studied here that could help to elucidate their ice nucleation activities. In addition, by employing a single-particle mass spectrometer, the degree of heterogeneity in the chemical composition within a given charcoal type (aerosol population) can be assessed. This is important for complex aerosols such as biomass burning particles, which often contain variable amounts of organic carbon, elemental carbon, and inorganic material. A total of 11 135 and 12 357 single-particle mass spectra were obtained for grass charcoal and wood charcoal, respectively.

3 Results and discussion

3.1 Ice nucleation ability

Figure 1 shows the AF of wood and grass charcoal as a function of temperature (230–255 K) relevant for MPC conditions, as obtained from the IMCA-ZINC experiments. The 400 nm diameter wood charcoal and grass charcoal particles showed a similar ice nucleation activity in this range, with the AF curves overlapping for both samples within experimental uncertainties, revealing a low immersion freezing ability overall. Specifically, values of $\mathrm{AF} \leq 0.1$ were observed at $T > 237$ K for both wood charcoal and grass charcoal particles. At $T < 237$ K, the AF increased, reaching values of around 0.59 and 0.66 for wood charcoal and grass charcoal particles, respectively, at $T = 235$ K, i.e., at the homogeneous ice nucleation temperature (HNT) of small pure water droplets. We indicate the homogeneous freezing conditions in Fig. 1 with the gray shading, using the parametrization of Earle et al. (2010). As the temperature in ZINC was further decreased below the HNT, the AF for both charcoal types increased, reaching maximum values of up to ~ 0.96 at $T = 231$ K. We note that particles leaving the aerosol lamina within ZINC, outside of which they are exposed to different conditions of T and RH, can cause AF values below unity (DeMott et al., 2015; Garimella et al., 2017). The sharp increase in AF below temperatures of 237 K likely results from homogeneous freezing of soluble organic or inorganic material associated with the charcoal particles. Given that the maximum temperature during pyrolysis of the initial biomass material was 450 °C, most of the organics should have vaporized (Stratakis and Stamatelos, 2003) and carried away with the N_2 purge flow during pyrolysis. Hence, the increase in AF observed in our freezing experiments is likely caused by soluble inorganic material. This is further corroborated by the mass spectral signatures obtained from our ATOFMS sampling discussed below. Overall, we conclude from our experiments shown in Fig. 1 that the charcoal particles investigated here are poor immersion mode INPs.

At first sight, our results appear in contrast to those of earlier studies that reported the appreciable immersion freezing activity of biomass burning particles, as discussed above. One way to reconcile the results reported here with those of previous studies is by considering the particle surface area per droplet used to study the immersion freezing activity of biomass burning particles that catalyzes their heterogeneous freezing activities. By accounting for the particles surface area, the AF values observed in our experiments can be normalized, and values of ice-active surface site density, n_{s} (e.g.,

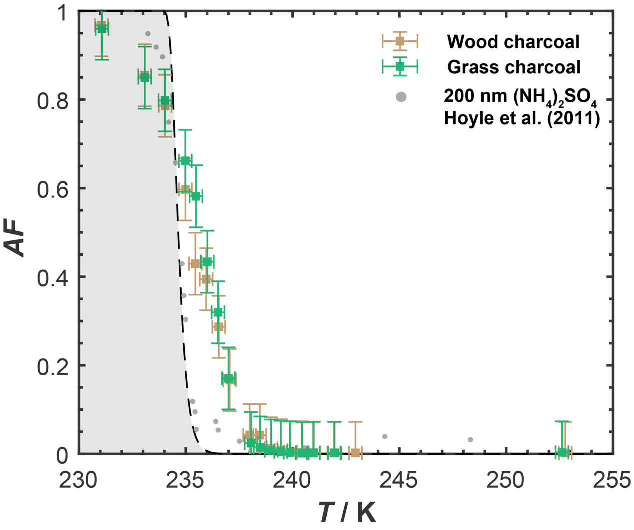

Figure 1. Mean activated fraction (AF) of $d_\mathrm{m} = 400$ nm charcoal particles as a function of temperature, as determined with IMCA-ZINC. The gray shaded region indicates homogeneous freezing conditions based on Earle et al. (2010). Error bars denote the uncertainty in the activated fraction due to particle counts of the CPC and OPC. Also shown are freezing data for 200 nm ammonium sulfate particles from Hoyle et al. (2011) for reference.

Vali, 2014), can be determined for our experiments. The n_s values of our experiments can then be directly compared to those of previous studies, with larger n_s values of a sample and at a given temperature, indicating higher (heterogeneous) ice nucleation activities. We note that the normalization to the surface area and comparisons among different studies only works under the assumption that the particle composition does not change with particle size. Nonetheless, the idea that an atmospherically relevant amount of particle surface area is present per droplet is an important parameter for evaluating ice nucleation. This is because the presence of large particles and large surface areas in a chemically inhomogeneous sample can trigger ice nucleation that would otherwise be absent in submicron aerosol particles in the submicron range that are typically present in cloud droplets.

Assuming spherical particle geometry for our particles, one 400 nm charcoal particle immersed in a single droplet has a surface area of $\sim 0.5\,\mu\mathrm{m}^2$. This value likely denotes an underestimation of the (true) particle surface area due to the complex morphology of the charcoal aerosols. Instead, a more realistic surface area value can be estimated by using the N_2-based BET-specific surface area of the charcoal types reported in Hammes et al. (2006; $2.0\,\mathrm{m}^2\,\mathrm{g}^{-1}$ for wood charcoal, $5.9\,\mathrm{m}^2\,\mathrm{g}^{-1}$ for grass charcoal), together with typical charcoal particle densities of $0.75\,\mathrm{g\,cm}^{-3}$ (Sander and Gee, 1990). Using these values and again assuming particle sphericity, we estimate surface areas of ~ 50 and $140\,\mu\mathrm{m}^2$ for a 400 nm diameter wood and grass charcoal particle, respectively. The surface area values of 50 and $140\,\mu\mathrm{m}^2$ together with the measured AF translate into n_s values of ~ 10 to $80\,\mathrm{cm}^{-2}$ at $T = 244$ K, which can be compared to those reported by other studies. We note that previous studies that have found biomass burning particles to be efficient immersion freezing nuclei were mostly performed on polydisperse combustion aerosol populations or by using droplets in cold stage techniques. In such cases, each droplet can contain multiple biomass burning particles. Thus, the particle (or INP) surface area per droplet is considerably larger in such cases, increasing the freezing probability compared to our measurements. As an example, Jahn et al. (2020) reported n_s values of approximately $8.10^3\,\mathrm{cm}^{-2}$ for their most ice-active ash sample tested and at their lowest temperature investigated of $T = 244$ K (see their Fig. 1b), which is several orders of magnitude higher than the n_s values of our experiments at the same temperature (~ 10 to $80\,\mathrm{cm}^{-2}$ at $T = 244$ K). This comparison illustrates that the surface area of charcoal particles per droplet in our experiments was likely insufficient to catalyze immersion freezing. Therefore, we conclude that biomass burning particles with properties (composition and surface area) similar to the pyrolysis-derived charcoal types studied here can likely not compete with the immersion freezing abilities of other atmospheric aerosol particles, such as mineral dust (e.g., Murray et al., 2012). In addition, we acknowledge that different physiochemical properties of the pyrolysis-derived charcoal particle types studied here compared to combustion-derived biomass burning particles investigated in other studies can further contribute to differences in observed ice nucleation activities.

Although the 400 nm diameter charcoal particles showed negligible immersion freezing activity, they revealed an enhanced ice nucleation ability at temperatures below the HNT. In Fig. 2, we show the complete AF curves for the different cirrus temperatures investigated here, as obtained from our RH scans performed in HINC. At $T < 233$ K, the charcoal particles showed a considerable ice nucleation activity for $\mathrm{RH} < \mathrm{RH_{hom}}$, where $\mathrm{RH_{hom}}$ denotes conditions for homogeneous freezing of aqueous solution droplets (indicated by the black dashed lines in Fig. 2). In addition, we observed different ice nucleation activities between the grass charcoal and the wood charcoal particles, with the latter being overall more ice-active at the cirrus temperatures investigated. As an illustration, the ice nucleation onset (corresponding to conditions where a value of $\mathrm{AF} = 10^{-2}$ is reached) at 218 K was as low as $\mathrm{RH_w} = 78\,\%$ ($130\,\%\ \mathrm{RH_i}$) for the wood charcoal particles, but for the grass charcoal particles, the onset was observed around 83 % ($138.5\,\%\ \mathrm{RH_i}$). We discuss these observed differences in more detail, deriving support from the auxiliary measurements.

As far as the ice nucleation activity of the charcoal particles in the cirrus temperature regime is concerned, we interpret this to result from a pore condensation freezing mechanism (PCF; Christenson, 2013; David et al., 2019; Fukuta, 1966; Higuchi and Fukuta, 1966; Koop, 2017; Marcolli, 2014). During PCF, water is taken up into pores and cracks

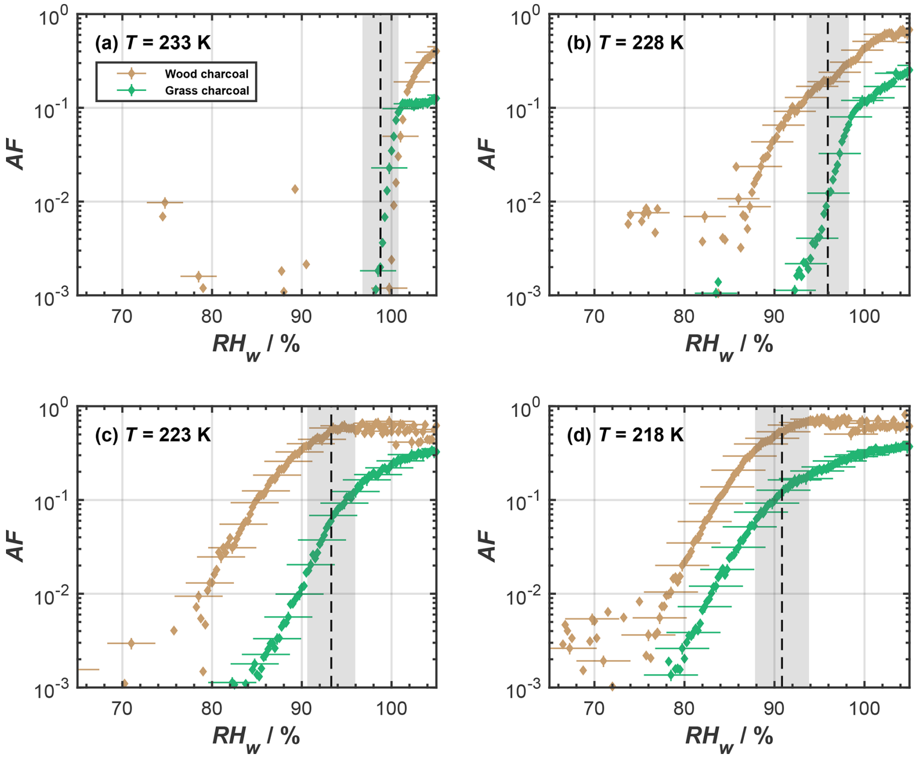

Figure 2. Mean activated fraction (AF) as a function of RH_w of the different size-selected charcoal particles ($d_m = 400$ nm), as determined from relative humidity scans in HINC for the cirrus regime temperatures of **(a)** 233 K, **(b)** 228 K, **(c)** 223 K, and **(d)** 218 K. The black dashed lines represent the expected homogeneous freezing conditions, according to Koop et al. (2000), and the gray shaded regions indicate the calculated RH_w variation across the aerosol lamina in HINC (Mahrt et al., 2018). Uncertainties are only given for every fifth data point for clarity.

available on the charcoal particles below water saturation, by capillary condensation, due to the lower-equilibrium vapor pressure in confined spaces, compared to bulk liquid water (Kelvin effect; e.g., Marcolli, 2014; Fisher et al., 1981). At $T \leq$ HNT this pore water can freeze homogeneously. Once formed, the microscopic pore ice can grow out of the pore to form macroscopic ice crystals (David et al., 2019; Koop, 2017), which can be detected in our cirrus temperature experiments with the OPC. An ice formation mechanism on charcoal via PCF is consistent with recent studies reporting PCF as the dominant ice formation mechanism for other combustion particle types including ash (Umo et al., 2019; Kilchhofer et al., 2021) and soot (Mahrt et al., 2018; Nichman et al., 2019; Jantsch and Koop, 2021; Marcolli et al., 2021; Gao et al., 2022a). Ice formation via PCF is strongly determined by the aerosol physicochemical properties (Marcolli et al., 2021; David et al., 2020). For instance, the study by David et al. (2020) showed that when investigating different synthetic silica particles with well-defined pore diameter and varying their surface functional groups to mimic different contact angles, during PCF, the pore filling with liquid water and ice growth out of the pore is largely controlled by the pore size and the contact angle between water or ice and the particle surface (making up the pore wall material). Additional RH scans performed with HINC at temperatures of 243 and 238 K (see Fig. A1) confirmed the absence of ice formation below water saturation for $T >$ HNT. Such a distinct increase in the ice formation ability at $T \leq$ HNT cannot be explained by a classical nucleation theory assuming ice formation via deposition nucleation, where a liquid water phase is absent (Welti et al., 2014). Thus, the marked dependence of ice formation on HNT suggests that the charcoal particles investigated herein form ice via PCF, where ice formation proceeds via the homogeneous freezing of liquid water in pores for $RH_w < 100$ %. These interpretations are consistent with the observations of previous studies (e.g., David et al., 2019). We further point out that the absence of ice nucleation for $RH < RH_{hom}$ at $T = 233$ K is not inconsistent with PCF but is explained by accounting for the negative pressure (tension of the water meniscus) experienced by the capillary condensate, i.e., the supercooled pore water (Marcolli, 2020). Marcolli (2020) demonstrated that, at temperatures close to the HNT, capillary condensates within pores only form close to water saturation. At these humidity conditions, the pore water experiences almost ambient pressure conditions, i.e., hardly any negative pressure. In turn, this causes the homogeneous ice nucleation rates to be lower compared to the cases at 228, 223, and 218 K, where we observed ice nucleation on the charcoal particles at considerably lower relative humidities and below homogeneous freezing conditions (see Fig. 2). At these temperatures, the charcoal pores fill at lower RH compared to the case of $T = 233$ K; hence, the pore water experiences higher negative pressures (Marcolli, 2020) and therefore higher homogeneous ice nucleation rates. We thus conclude that, at $T = 233$ K, the homogeneous ice nucleation rates are too low to observe ice formation within the particle residence time of ~ 10 s within HINC (David et al., 2019; Marcolli, 2020).

Altogether, the high ice supersaturations required to nucleate ice on these particles at $T = 233$ K, and the absence of (strong) heterogeneous ice formation at $T > 233$ K (Figs. 1 and A1), render it unlikely that ambient aerosols with physicochemical properties similar to the pyrolysis-derived charcoal particles investigated here contribute to heterogeneous ice nucleation at $T >$ HNT. Yet, at $T \leq$ HNT, the charcoal particles revealed heterogeneous ice nucleation at conditions well below those relevant for homogeneous freezing of solution droplets, making the charcoal particles investigated here considerably better cirrus ice nuclei compared to other biomass-burning-derived particles investigated earlier (DeMott et al., 2009).

3.2 Water vapor sorption

Figure 3a shows the water vapor sorption and desorption isotherms of the two charcoal samples, as determined by DVS experiments. These measurements allow us to simultaneously infer information on the charcoal hydrophilicity and porosity. During DVS, water uptake and loss is determined gravimetrically, and in Fig. 3a, we show the mass change, Δm, denoting the quasi-equilibrated (steady-state) moist sample mass at each $\mathrm{RH_w}$ value relative to the dry sample mass at 0 % $\mathrm{RH_w}$. The solid lines and filled symbols in Fig. 3a represent water uptake isotherms, and the dashed lines and open symbols represent the water loss isotherms for the same DVS run.

The grass charcoal sample exhibits a shallow water uptake curve up to 80 % $\mathrm{RH_w}$, with $\Delta m < 0.5$ %. The corresponding water-vapor-based, BET-specific surface area of the grass charcoal sample was determined as $\mathrm{BET_{H_2O}} = 7.9\ \mathrm{g\,m^{-2}}$ (see Appendix D). Between 83 % and 98 % $\mathrm{RH_w}$, the grass charcoal shows a more pronounced water uptake, with a maximum in Δm of around 3 % being reached at the largest $\mathrm{RH_w}$ value (98 % $\mathrm{RH_w}$). The absence of a plateau at these high $\mathrm{RH_w}$ levels suggests that the formation of a water multilayer and free water would occur if the $\mathrm{RH_w}$ was further increased. We interpret the gradual curvature of the water uptake observed for the grass charcoal as a type II isotherm, following the IUPAC (International Union of Pure and Applied Chemistry) classification recommendations (Thommes et al., 2015; Sing et al., 1985). Type II isotherms are given by the reversible physisorption of gases on macroporous adsorbents, as discussed in detail elsewhere (Thommes et al., 2015). While type II isotherms are characteristic of macroporous (pore diameter >50 nm) adsorbents, the abrupt change in water uptake around 83 % and the enhanced water uptake at higher $\mathrm{RH_w}$ indicates some water uptake by the filling of mesopores (pore diameter between 2 and 50 nm, Thommes et al., 2015). The presence of mesopores on the grass charcoal is further supported by the (weak) hysteresis observed between the water uptake and the water loss curves. The presence of mesopores is consistent with (weak) PCF ice formation observed for the grass charcoal particles at some cirrus temperatures (Fig. 2; $T \leq 223$ K). The hysteresis of the grass charcoal is typical of a H3-type hysteresis, which is often observed for adsorbents with a type II adsorption isotherm (Thommes et al., 2015). Nonetheless, we note that, overall, the observed hysteresis is weak; thus, the deviation from an idealized type II isotherm, where adsorption is assumed to be fully reversible, is low. This indicates that, while some mesopores are present on the grass charcoal particles, this sample is likely dominated by macropores. A H3-type hysteresis loop and a dominance of macropores is characteristic for aggregates of plate-like particles (Thommes et al., 2015). A plate-like particle morphology for the charcoal aerosols is qualitatively supported by our TEM images, as shown in Fig. 3b (see also Fig. C1), and is, furthermore, consistent with previous studies reporting that charcoal particles mostly sustain the shape of the fuel material to some degree (Sharma et al., 2004).

The wood charcoal sample shows a distinctively different water uptake and loss behavior compared to the grass charcoal sample. Specifically, the water uptake curve of the wood charcoal reveals a pronounced concave curvature with an initial steep increase reaching values of $\Delta m = 6.5$ % at 40 % $\mathrm{RH_w}$ and a more gradual uptake as the $\mathrm{RH_w}$ is further increased. We attribute this to a type IV(a) isotherm (IUPAC classification recommendation). Nonetheless, we note that a final saturation plateau at high $\mathrm{RH_w}$, a typical feature associated with type IV(a) isotherms (Thommes et al., 2015), was not observed for the wood charcoal sample. The strong increase in sample mass at very low $\mathrm{RH_w}$ is a common feature of samples that have micropores (pore diameter <2 nm Thommes et al., 2015) and/or a large specific surface area. The $\mathrm{H_2O}$-based, BET-specific surface area of the wood charcoal sample corresponding to the water uptake isotherm of our DVS measurement was determined to be $\mathrm{BET_{H_2O}} = 161.3\ \mathrm{g\,m^{-2}}$ (see Appendix D). A similar adsorption behavior has previously been reported for microporous combustion particles (e.g., Popovitcheva et al., 2000; Popovicheva et al., 2008). The relatively broad $\mathrm{RH_w}$ range over which the concave shape of the water uptake isotherm extends in our experiment suggests a broad range of differently sized micropores. We note that such micropores are negligible for ice formation via PCF because micropores are too narrow to accommodate a critical ice embryo needed for ice formation when using classical nucleation theory to estimate the size of a critical spherical ice cluster. In fact, in

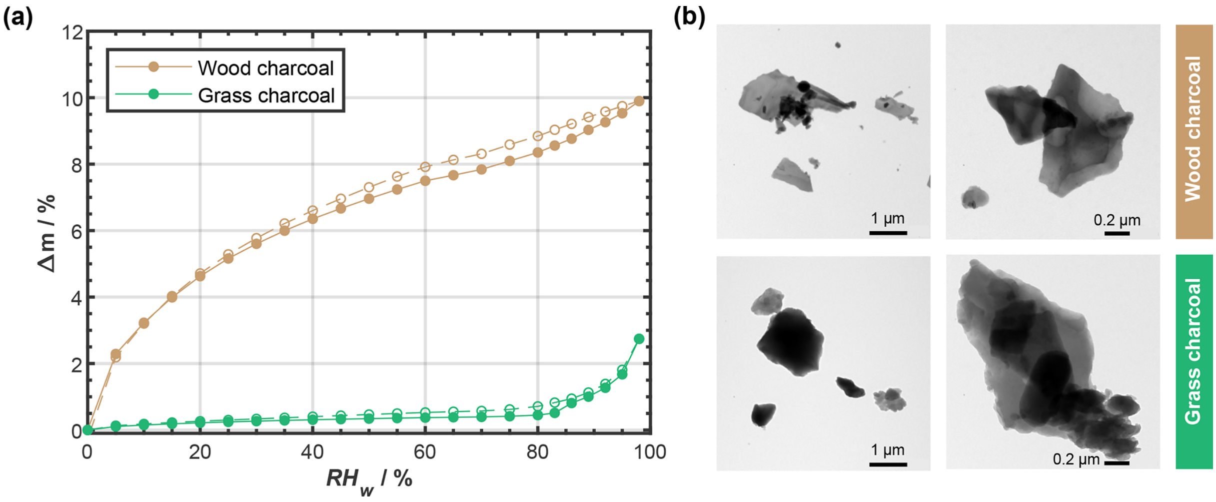

Figure 3. **(a)** Water uptake (solid lines; filled symbols) and loss (dashed lines; open symbols) isotherms given as relative sample mass change, Δm, as a function of relative humidity with respect to water (RH_w), as determined by dynamic vapor sorption. Sorption isotherms were measured at $T = 298$ K, and the data points represent water uptake and loss at quasi-equilibrated RH_w conditions. Lines are to guide the eye, and uncertainty in Δm is 0.75 %. **(b)** Example transmission electron microscopy images of wood charcoal and grass charcoal.

a previous study, the smallest pore for which ice nucleation was experimentally observed, in a setup similar to the one used here, had a radius of $r = 1.25$ nm (David et al., 2020). Nonetheless, our DVS measurements also contain characteristic features that indicate the presence of mesopores on the wood charcoal particles. Specifically, the initial increase in water mass along the water uptake curve of the wood charcoal initially proceeds via a similar path as the corresponding part of the type II isotherm of the grass charcoal, even at higher water masses. At around 40 % RH_w, the water uptake rate increases, indicating pore condensation. In addition, the wood charcoal DVS measurements are accompanied by a clear hysteresis, typical of type IV(a) isotherms, and absent in the case of type IV(b) isotherms (Thommes et al., 2015). We attribute this hysteresis to a H4-type hysteresis that is typical of micro- and mesoporous carbonaceous material (Thommes et al., 2015). The availability of mesopores on the wood charcoal sample supports our interpretation of ice formation via PCF on these particles, as described above.

Overall, our DVS measurements reveal that the wood charcoal samples show a higher water uptake capacity compared to the grass charcoal sample. For instance, at 98 % RH_w, the water uptake of wood charcoal is approximately a factor of ∼ 4 larger compared to the grass charcoal sample. We interpret the higher water affinity of the wood charcoal sample compared to the grass charcoal to result partly from a lower charcoal–water contact angle of the former, which is consistent with the larger ice nucleation activity of the wood charcoal particles at $T <$ HNT (see Fig. 2). However, we point out that the difference in (PCF) ice nucleation activity observed between the wood charcoal and grass charcoal is not constant across the cirrus temperatures investigated here, indicating that it is not directly proportional to the hydrophilicity and mesopore volume observed in the DVS measurements. This is consistent with previous DVS measurements and (PCF) ice nucleation observations for soot particles (Mahrt et al., 2020) and suggests that other aerosol properties such as the chemical composition might need to be considered in order to explain the observed ice nucleation activity.

3.3 Chemical composition

Figure 4 shows a summary of the chemical composition of the charcoal particles, as obtained from our ATOFMS sampling. Depicted are the average anion and cation stick spectra of grass charcoal and wood charcoal, respectively, where the peaks denote average ion intensities in terms of the relative overall peak area particles that resulted in a detectable ion signal upon being hit with the Nd:YAG laser. Major peaks with relative area signals larger than or equal to 0.02 are labeled for clarity. We point out that the ATOFMS is a semi-quantitative instrument and that the relative peak intensities do not correspond to the actual mass fraction of the respective component.

The anion spectrum of grass charcoal (Fig. 4a) is marked by peaks of organic ions, including the typical C_n fragmentation (C_1^-–C_5^-; m/z 12 … 60), and peaks occurring at 25 (C_2H^-), 26 ($C_2H_2^-$/CN^-), 27 ($C_2H_3^-$/NCH^-), 49 (C_4H^-), and 50 ($C_4H_2^-$). The presence of a peak at 46 (NO_2^-), although at very low relative intensity, renders the presence of nitrogen-containing ions at m/z of 26 (CN^-) and 27 (NCH^-) possible, which is further supported by the peak at 42 (CNO^-). Ion peaks at 26 (CN^-) and 42 (CNO^-) have previously been used as an indicator of biological aerosol (Sierau et al., 2014; Creamean et al., 2013; Pratt et al., 2009), which should be absent in the charcoal particles used here.

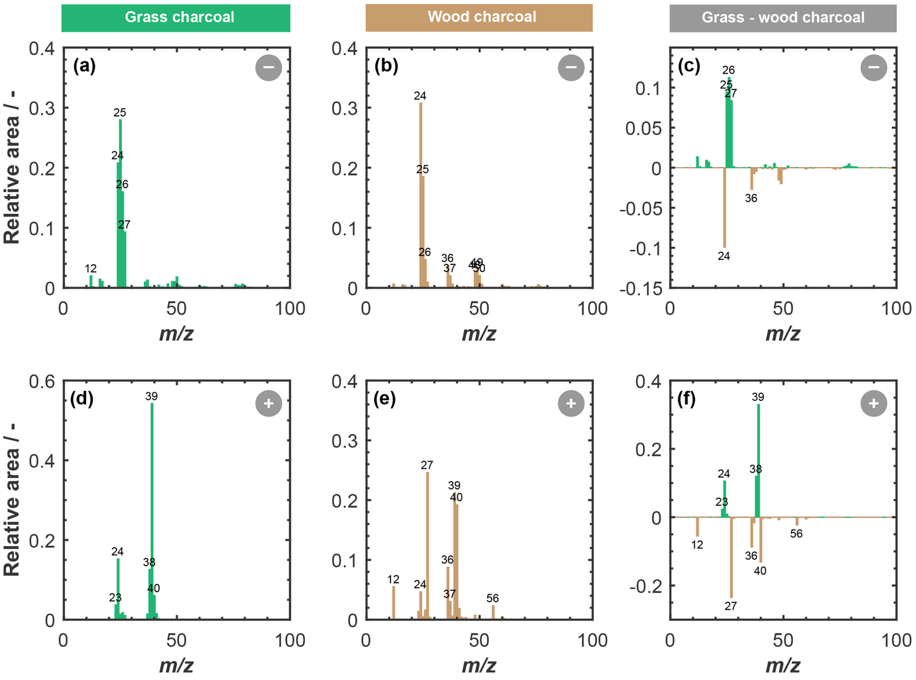

Figure 4. Average ATOFMS mass spectra for grass charcoal particles and wood charcoal particles for different polarities, including negative mass spectra for **(a)** grass charcoal and **(b)** wood charcoal and positive mass spectra for **(d)** grass charcoal and **(e)** wood charcoal. The panels in the right-hand column compare the two charcoal types and show the difference in the relative peak area for the wood charcoal signal being subtracted from the grass charcoal for anions and cations, respectively. A positive (negative) signal in panels **(c)** and **(f)** corresponds to a larger (lower) relative peak area signal of the respective ions for the grass charcoal compared to the wood charcoal. All spectra are shown in terms of relative peak area and for unit mass resolution. Each single-particle spectrum was first normalized, and then the average was calculated over 11 135 (grass) and 12 357 (wood) spectra. Peaks with relative area signals larger than 0.02 are labeled with the corresponding mass to charge (m/z) ratio.

Thus, the anion peaks at m/z of 26 and 27 in our average grass charcoal spectra are more likely attributable to hydrocarbons ($C_2H_2^-$ and $C_2H_3^-$, respectively) or less likely, but still possible, organic nitrogen (CN^- and HCN^-), consistent with these peaks being previously been observed for cellulose particles and particles from biomass burning (Schmidt et al., 2017). The small peak at 97 (HSO_4^-; low relative intensity $\ll 0.1$) suggests the presence of further secondary material on the grass charcoal particles. Additionally, the grass charcoal contains a small peak at 79 (PO_3^-). Overall, these peaks are all typical marker ions occurring in aerosol particles from biomass burning emissions (Schmidt et al., 2017; Zawadowicz et al., 2017).

Characteristic marker peaks for biomass burning aerosol are also found in the average cation spectrum of the grass charcoal (Fig. 4d), including peaks at 23 (Na^+), 24 (C_2^+), and 40 ($Ca^+/NaOH^+$). Yet, another ion typically occurring in biomass burning aerosol is potassium (K^+, m/z 39), whose peak is dominating the average cation spectrum of grass charcoal. This is consistent with previous studies showing that mass spectra obtained by ablation and ionization mass spectrometers are often dominated by ions with low ionization efficiencies such as alkali metals (Zelenyuk and Imre, 2005). In addition, the ionization efficiency can be impacted by the particle matrix in laser ablation mass spectrometry (Gross et al., 2000; Reilly et al., 2000) and the particle size and morphology (Kane and Johnston, 2000). We further note that non-uniform ablation and ionization, e.g., due to the Gaussian intensity profile of the Nd:YAG laser beam, can cause the resulting mass spectrum to not contain information on the entire particle composition (Ge et al., 1998), making the ATOFMS analysis a semi-quantitative method, as noted above. In Fig. B1, we show the mass spectra depicted in Fig. 4 in a complementary way, to better reflect the variation in the relative peak area across the entire charcoal particle population. Specifically, Fig. B1 shows what fraction of the investigated particles contained a certain ion species, together with the relative ion signal intensity. Even though there is some variation in the relative peak intensities, we note that a considerable fraction of the charcoal particles contains the characteristic (average) ion peaks shown in Fig. 4. Thus, we conclude that the variability in chemical composition within a given charcoal types is sufficiently low and that the average spectra shown in Fig. 4 provide a reasonable picture of the composition of the particles investigated here. The number size distributions of the particles contributing to the average spectra in Figs. B1 and 4 are shown in Fig. B2. For both charcoal types, the mode of the particle size distribution is in the submicrometer range, between 300 to 500 nm (vacuum aerodynamic diameter). Thus, we consider the average spectra shown in Fig. 4 to be representative of the 400 nm charcoal particles used for our ice nucleation experiments.

The average anion spectrum of the wood charcoal is shown in Fig. 4b. The wood charcoal particles contained typical marker ions at C_1^-–C_6^- (m/z 12 … 72) and associated hydrocarbon peaks at 25 (C_2^-), 26 ($C_2H_2^-$), 37 (C_3H^-), 49 (C_4H^-), 50 ($C_4H_2^-$), 51 ($C_4H_3^-$), 52 ($C_4H_4^-$), 73 (C_6H^-), and 74 ($C_6H_2^-$), although some of these peaks have relative areas below 0.1 (see Fig. B1c). In addition, peaks of secondary material were also present at 97 (HSO_4^-). A peak that was present in the anion spectrum of wood but not in grass charcoal appears at m/z of 76, which we attribute to $AlO_2(OH)^-$. Alumina species are known to contribute to the ice nucleation activity of ambient particles, as they form significant components of atmospherically relevant mineral particles such as illite, which are also known to be porous, ice-active aerosol particles (David et al., 2019; Hiranuma et al., 2015; Welti et al., 2009).

The presence of aluminum is further corroborated by the average cation spectrum of wood charcoal depicted in Fig. 4e, showing a prominent peak at 27 (Al^+). The presence of aluminum in the wood charcoal is compliant with earlier observations of McCluskey et al. (2014), who reported aluminum to be abundant in ice nucleation particles from wildfires, as noted above. Next to aluminum, the cation wood charcoal spectrum indicates the presence of other metals ions such as 56 (Fe^+). Also present are peaks at 23 (Na^+), 24 (Mg^+), and 40 (Ca^+). These peaks are characteristic for mineral material and have previously been reported for, e.g., dust samples (e.g., Gallavardin et al., 2008; Marsden et al., 2019). The presence of calcium and magnesium within our charcoal particles is also consistent with recent results of Adachi et al. (2022), who have reported these species to be important components of (fine) ash particles emitted by biomass burning.

The cation spectrum of wood charcoal is characterized by the presence of 39 (K^+) and a C_n fragmentation pattern (C_1^+–C_3^+; m/z 12, 24, and 26). Overall, the peaks observed in the anion and cation spectrum of wood charcoal contain ions often observed in spectra of fly ash particles, as reported previously (Zawadowicz et al., 2017; Grawe et al., 2018; Xu et al., 2018). For example, similar peaks have previously been reported by Grawe et al. (2018) when sampling aerosol particles from different ash types sourced from coal-burning power plants and also measured with a single-particle mass spectrometer, where more than 80 % of all particles samples (across all ash types) contained peaks at 27 (Al^+) and 40 (Ca^+). Similarly, recent findings have demonstrated inorganics (Ca and Mg) to be abundant in ash particles from biomass burning (Adachi et al., 2022).

Overall, our ATOFMS results clearly reveal the presence of mineral components in the wood charcoal particles. The availability of mineral ions in the wood charcoal correlates positively with their enhanced ice nucleation activity compared to the grass charcoal particles, where ion signatures characteristic for mineral components were largely absent in the average mass spectra. These results parallel the recent findings by Jahn et al. (2020) that combustion-derived minerals, resulting from transformation of inorganic material that is naturally present within the fuel material, might govern the ice nucleation activity of particles emitted by biomass burning. This is further supported by other studies suggesting that inorganic or mineral components to play a key role in the ice nucleation activity of particles emitted by biomass burning (Petters et al., 2009; Jahl et al., 2021; McCluskey et al., 2014). At the same time, we acknowledge that, while our ATOFMS analysis provides valuable information on the chemical composition of the charcoal particles, including their refractory components, a detailed chemical mechanism by which these minerals promote their ice nucleation activity cannot be explicitly derived here, given the correlational nature of our data. Moreover, the presence of some cirrus ice nucleation activity for the grass charcoal particles, where mineral signatures were largely absent, underscores the need for future studies to better understand the relative importance of pores and active (mineral) sites for the ice nucleation activity of charcoal particles and biomass burning particles in general.

4 Summary and conclusions

In this study, we investigated the ice nucleation ability of charcoal particles, an important class of aerosols generated during biomass combustion. Two charcoal samples were tested, as derived from pyrolysis of relevant biomass types, namely wood and grass charcoal. Ice nucleation experiments were carried out on 400 nm size-selected particles. Such submicron charcoal particles are expected to be transported into higher altitudes (Clark and Hussey, 1996; Gilgen et al., 2018) where they can affect cloud formation. Ice nucleation activities were tested over a temperature range of $218\,\mathrm{K} \leq T \leq 253\,\mathrm{K}$. In the MPC regime ($T > 233\,\mathrm{K}$), the ice nucleation was tested in immersion freezing mode, while for the cirrus temperatures ($T \leq 233\,\mathrm{K}$), RH scans were performed, covering a range of RH_w (RH_i) 65 %–105 % (100 %–180 %). The bulk aerosol water uptake and loss were characterized gravimetrically by means of dynamic water vapor sorption (DVS) measurements, allowing the inference of material porosity, and the chemical composition of the particles was characterized using a single-particle aerosol time-of-flight mass spectrometer (ATOFMS).

We found that the 400 nm charcoal particles investigated here were poor immersion freezing INPs at MPC temperatures and independent of the charcoal type, even in the presence of mineral components. In comparison to previous studies that often reported some immersion freezing of biomass burning particles, we attributed this to the small particle (INP) surface area available per droplet in our experiments. By contrast, at cirrus temperatures, we found a considerable heterogeneous ice nucleation ability of the pyrolysis-derived charcoal particles at relative humidities below those required for homogeneous freezing of solution droplets. This dependence of the ice formation ability on the homogeneous ice nucleation temperature of pure water droplets (HNT = 235 K) provides ample evidence that ice nucleation on charcoal proceeds via a pore condensation and freezing (PCF) mechanism. At $T < 233$ K, the observed ice nucleation activity was higher for wood charcoal compared to grass charcoal particles. In this temperature range, the cirrus ice nucleation activity correlated with both physical and chemical particle properties. In terms of physical properties, the ice nucleation activity positively correlated with the particle porosity. Specifically, the wood charcoal particles showed higher porosity and water uptake capacity, consistent with the higher ice nucleation activity via PCF of the wood charcoal compared to the grass charcoal. In terms of particle chemical properties, the cirrus ice nucleation activity positively correlated with the presence of inorganic mass spectral features. More specifically, the mass spectra of the wood charcoal particles contained ions indicating the presence of mineral components that were mostly absent in the mass spectra of the grass charcoal. This is consistent with findings of earlier studies that reported ice active particles generated from combustion processes to contain mineral components (Jahn et al., 2020; Petters et al., 2009; Grawe et al., 2018) and other studies that have reported mineral components of other aerosol types to nucleate ice (e.g., Archuleta et al., 2005).

Overall, we found considerable similarities in the grass and wood charcoal average mass spectra with those reported in the literature for particles classified as biomass burning particles and (coal) fly ash particles, respectively. This could indicate that charcoal particles, as studied here, are atmospherically more widespread and abundant than previously thought. This is corroborated by recent findings of Adachi et al. (2022), who reported fine ash particles (classified by the authors as particles having Ca and Mg > 0.5 wt %) to be a major constituent associated with biomass burning and estimated their global emission to range between 8.8 and 16.3 Tg yr^{-1}. Taken together, these studies reveal that clear identification, differentiation, and quantification of the various particle types associated with complex biomass burning emissions remains a challenging task but is essential to confirm assumptions about their abundance and environmental effects made in models.

In this regard, we recognize that our results are confined to charcoal particles produced by low-temperature pyrolysis and hence cannot necessarily be generalized to all atmospheric charcoal particles and other particles emitted by biomass burning. Certainly, in real biomass burning events, the temperature can vary considerably (Mondal and Sukumar, 2014), thus affecting pyrolysis yields and particulate and gas product distributions (Demirbas, 2007; Safdari et al., 2019). For instance, Safdari et al. (2019) have reported that tar-like material makes up between 44 % and 62 % of weight of the particulate products when investigating the pyrolysis of 14 common plant species native to the United States; this is consistent with other work that has reported tar particles to be a dominant component of biomass burning emissions (e.g., Adachi et al., 2019). The interaction of charcoal particles with particulate and gas components co-emitted during biomass pyrolysis can alter their ice nucleation abilities. For example, tar-like material and condensing organic vapors can fill the pores available on the charcoal particles and hence render them inaccessible for PCF ice nucleation, an effect that has previously been observed for soot particles (e.g., Gao et al., 2022b; Zhang et al., 2020). Moreover, it was recently reported that biomass burning particles can undergo atmospheric aging processes, leading to removal of organic coatings that mask the aerosol's ice-active sites and ultimately enhancing their ice nucleation activity (Jahl et al., 2021). Such effects were absent for the charcoal particles studied here, as the organic vapors formed during pyrolysis were continuously removed in the experimental setup used do generate the particles, as described above.

Therefore, future measurements with more realistic charcoal particles, as studied here, are crucial to the further improve our understanding of their physical and chemical properties in relation to their cirrus ice nucleation activities. In particular, it will be important to better understand the role of organic material associated with atmospherically realistic charcoal particles in determining their ice nucleation activity and how this is impacted by atmospheric aging processes. Future studies are also needed to investigate the relative importance of the ice nucleation ability of pyrolysis-derived charcoal to that of other particle types emitted during biomass burning. Particular focus should be put on investigating the ice nucleation abilities of such particles at cirrus temperatures, where available data remain limited.

In the present study, we avoided generalizations about the relative importance of physical over chemical particle properties in determining ice nucleation activities, given the correlational nature of our ice nucleation results and the physicochemical particle properties investigated here. Furthermore, in view of INPs making up only a small fraction of the total aerosols emitted, correlations with bulk particle properties should be interpreted carefully. Therefore, for future studies it will also be crucial to more holistically understand the physical and chemical properties of the highly complex biomass burning aerosol on the level of single particles that form and do not form ice. Such analysis could be achieved by examining ice crystal residual particles, to attribute the ice nucleation activity to their properties with more certainty and disentangle their relative contributions and importance, by comparing them to properties of interstitial particles that did not form ice crystals.

Appendix A: Ice nucleation

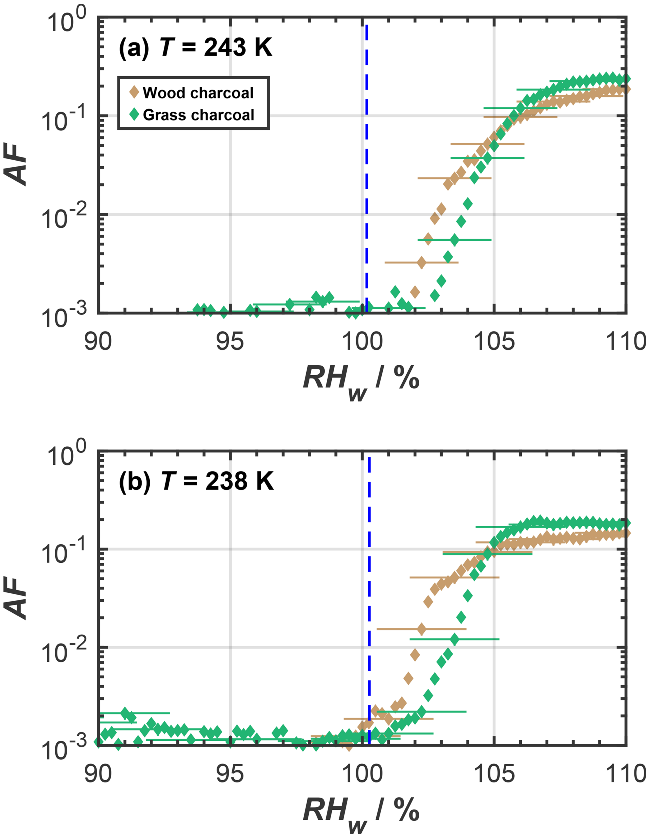

Figure A1. Mean activated fraction (AF) as a function of RH_w of size-selected charcoal particles ($d_m = 400$ nm), as determined from relative humidity scans in HINC for mixed-phase cloud temperatures of **(a)** 243 K and **(b)** 238 K. The blue dashed lines represent water droplet survival for a particle of initial diameter of 400 nm, a residence (growth) time of 10 s, and assuming pure condensational growth, following Lohmann et al. (2016). Uncertainties are only given for every fifth data point for clarity.

Appendix B: Aerosol time-of-flight mass spectrometry

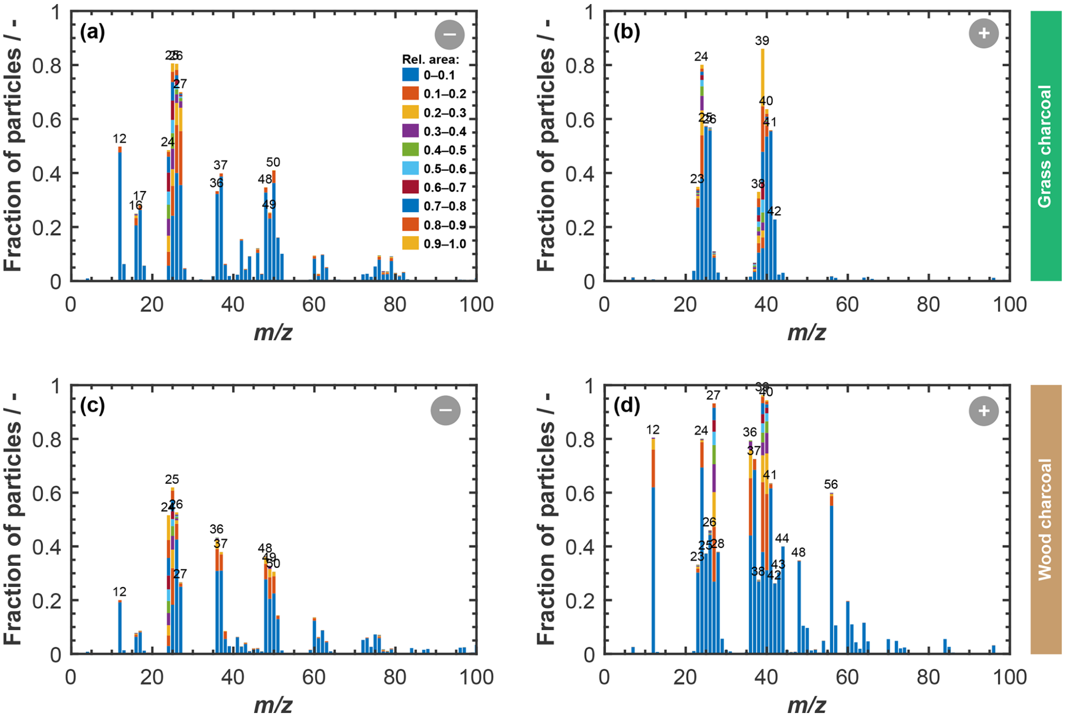

Figure B1. Average positive and negative ATOFMS mass spectra for grass charcoal **(a, b)** and for wood charcoal **(c, d)**. In each panel, the mass spectra are shown in terms of the fraction of particles out of all particles of a given charcoal type that contain a peak with relative peak area values as indicated by the color code shown in panel **(a)**.

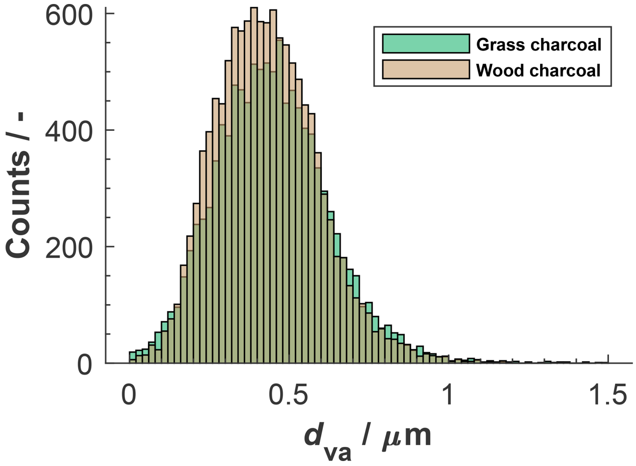

Figure B2. Histogram of particle size for grass and wood charcoal samples, based on the ATOFMS data, showing the vacuum aerodynamic diameter (d_{va}). Single-particle data were binned into 20 nm bins between 0 µm $< d_{\mathrm{va}} \leq 1.5$ µm.

Appendix C: Transmission electron microscopy

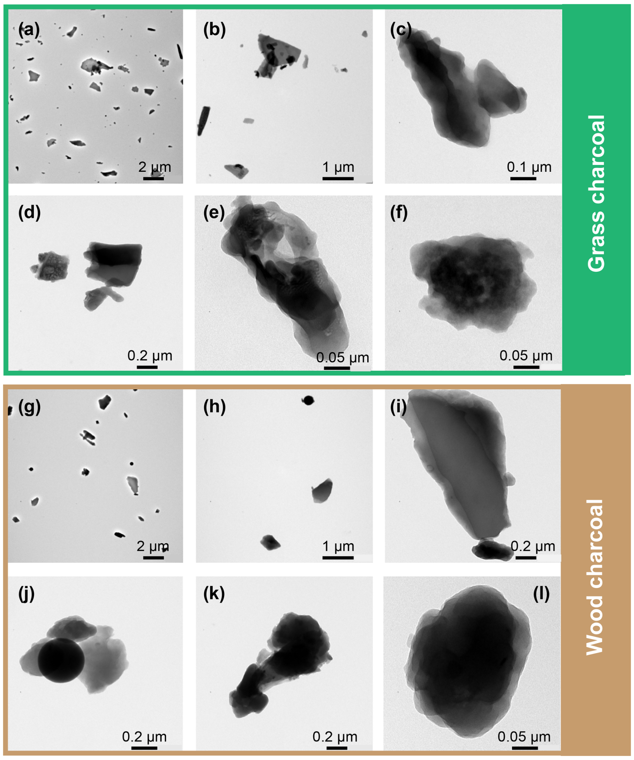

Figure C1. Exemplare transmission electron microscopy images of representative charcoal particles, sampled from a polydisperse aerosol population. Images show **(a)**–**(f)** grass charcoal particles and **(i)**–**(l)** wood charcoal particles, respectively.

Appendix D: Dynamic vapor sorption

The specific particle surface area was determined from the water vapor adsorption isotherms measured by DVS and using the BET method. Specifically, the surface area values were determined from the linear BET plot of the H_2O isotherm (Fig. D1) up to between $p/p_0 = 0.15$ and $p/p_0 = 0.35$, where p is the equilibrium pressure, and p_0 denotes the saturation vapor pressure, assuming a H_2O molecular cross-sectional area of $\sigma_{\mathrm{H_2O}} = 0.114\,\mathrm{nm}^2$ and using the linear form of the BET equation as follows (Thommes et al., 2015):

$$\frac{\frac{p}{p_0}}{\mathrm{n}(1-\frac{p}{p_0})} = \frac{\mathrm{C}-1}{n_\mathrm{m}C}\left(\frac{p}{p_0}\right)+\frac{1}{n_\mathrm{m}C}. \tag{D1}$$

Here n is the total amount of water vapor adsorbed on the particles, n_m is the specific monolayer capacity, and C is a constant. The water-vapor-based BET surface areas were determined as 161.3 and $7.9\,\mathrm{m}^2\,\mathrm{g}^{-1}$ for wood charcoal and grass charcoal, respectively.

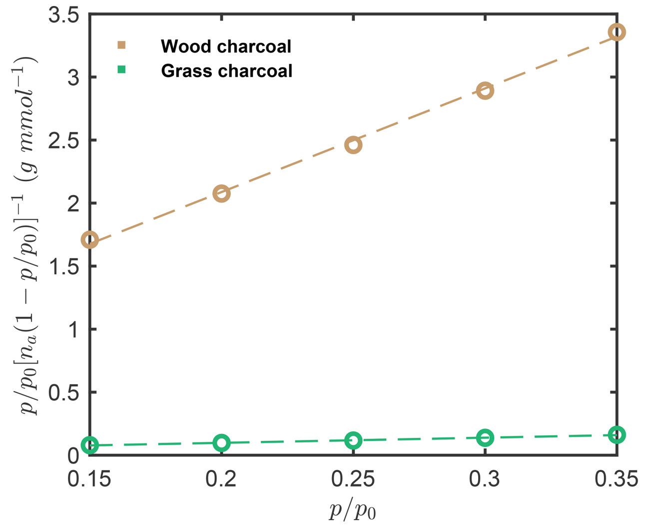

Figure D1. BET plot of the charcoal samples.

Code availability. The original FATES software package is available online at https://doi.org/10.5281/zenodo.398847 (Sultana et al., 2017a, b), and all future releases will be available at https://www.github.com/CMSultana/FATESmatlabToolKit (last access: 17 January 2023).

Data availability. The data in this paper can be found at https://doi.org/10.3929/ethz-b-000591583 (Mahrt et al., 2023).

Sample availability. Charcoal samples were obtained from Michael W. I. Schmidt at the University of Zurich, Switzerland, Department of Geography, and can be ordered using the following link: https://www.geo.uzh.ch/en/units/2b/Services/BC-material/Black-carbon-rich-materials.html (last access: 12 January 2023, Schmidt, 2023).

Author contributions. FM prepared all figures and wrote the initial draft with contributions from CR and ZAK. FM, CR, and ZAK designed the experiment. KG and FM conducted and analyzed HINC measurements. CR conducted and analyzed IMCA-ZINC measurements and sampled particles for TEM analysis. CD ran DVS experiments. FM sampled ATOFMS data. MAZ and FM analyzed and interpreted ATOFMS data. All authors contributed to data interpretation and to revising the paper.

Competing interests. The contact author has declared that none of the authors has any competing interests.

Disclaimer. Publisher's note: Copernicus Publications remains neutral with regard to jurisdictional claims in published maps and institutional affiliations.

Acknowledgements. The authors acknowledge Michael Schmidt, from the University of Zurich, for providing the charcoal samples (https://www.geo.uzh.ch/en/units/2b/Services/BC-material/Black-carbon-rich-materials.html, last access: 12 January 2023). David P. Fergenson is thanked, for technical support with the ATOFMS. This work has been supported by the atmospheric physics professorship at ETH Zurich. The authors further acknowledge the technical support of Hannes Wydler and Michael Rösch, with the experimental setup and maintenance. Furthermore, we thank Ingo Burgert, for providing access to the DVS facility, and Eszther J. Barthazy-Meier, for providing TEM images.

Financial support. This research has been supported by the ETH Zürich Foundation (grant no. ETH-25-15-1), the Horizon 2020 (MICROSCOPE; grant no. 890200), the Schweizerischer Nationalfonds zur Förderung der Wissenschaftlichen Forschung (grant no. 200021_156581), and the China Scholarship Council (grant no. 201906020041).

Review statement. This paper was edited by Qi Chen and reviewed by two anonymous referees.

References

Adachi, K., Sedlacek, A. J., Kleinman, L., Springston, S. R., Wang, J., Chand, D., Hubbe, J. M., Shilling, J. E., Onasch, T. B., Kinase, T., Sakata, K., Takahashi, Y., and Buseck, P. R.: Spherical tarball particles form through rapid chemical and physical changes of organic matter in biomass-burning smoke, P. Natl. Acad. Sci., 116, 19336–19341, https://doi.org/10.1073/pnas.1900129116, 2019.

Adachi, K., Dibb, J. E., Scheuer, E., Katich, J. M., Schwarz, J. P., Perring, A. E., Mediavilla, B., Guo, H., Campuzano-Jost, P., Jimenez, J. L., Crawford, J., Soja, A. J., Oshima, N., Kajino, M., Kinase, T., Kleinman, L., Sedlacek III, A. J., Yokelson, R. J., and Buseck, P. R.: Fine Ash-Bearing Particles as a Major Aerosol Component in Biomass Burning Smoke, J. Geophys. Res.-Atmos., 127, e2021JD035657, https://doi.org/10.1029/2021JD035657, 2022.

Adams, M. P., Tarn, M. D., Sanchez-Marroquin, A., Porter, G. C. E., O'Sullivan, D., Harrison, A. D., Cui, Z., Vergara-Temprado, J., Carotenuto, F., Holden, M. A., Daily, M. I., Whale, T. F., Sikora, S. N. F., Burke, I. T., Shim, J.-U., McQuaid, J. B., and Murray, B. J.: A Major Combustion Aerosol Event Had a Negligible Impact on the Atmospheric Ice-Nucleating Particle Population, J. Geophys. Res.-Atmos., 125, e2020JD032938, https://doi.org/10.1029/2020JD032938, 2020.

Adolf, C., Wunderle, S., Colombaroli, D., Weber, H., Gobet, E., Heiri, O., van Leeuwen, J. F. N., Bigler, C., Connor, S. E., Gałka, M., La Mantia, T., Makhortykh, S., Svitavská-Svobodová, H., Vannière, B., and Tinner, W.: The sedimentary and remote-sensing reflection of biomass burning in Europe, Glob. Ecol. Biogeogr., 27, 199–212, https://doi.org/10.1111/geb.12682, 2018.

Andreae, M. O. and Gelencsér, A.: Black carbon or brown carbon? The nature of light-absorbing carbonaceous aerosols, Atmos. Chem. Phys., 6, 3131–3148, https://doi.org/10.5194/acp-6-3131-2006, 2006.

Andreae, M. O. and Merlet, P.: Emission of trace gases and aerosols from biomass burning, Glob. Biogeochem. Cycles, 15, 955–966, https://doi.org/10.1029/2000GB001382, 2001.

Andreae, M. O., Anderson, B. E., Blake, D. R., Bradshaw, J. D., Collins, J. E., Gregory, G. L., Sachse, G. W., and Shipham, M. C.: Influence of plumes from biomass burning on atmospheric chemistry over the equatorial and tropical South Atlantic during CITE 3, J. Geophys. Res.-Atmos., 99, 12793–12808, https://doi.org/10.1029/94JD00263, 1994.

Archuleta, C. M., DeMott, P. J., and Kreidenweis, S. M.: Ice nucleation by surrogates for atmospheric mineral dust and mineral dust/sulfate particles at cirrus temperatures, Atmos. Chem. Phys., 5, 2617–2634, https://doi.org/10.5194/acp-5-2617-2005, 2005.

Barry, K. R., Hill, T. C. J., Levin, E. J. T., Twohy, C. H., Moore, K. A., Weller, Z. D., Toohey, D. W., Reeves, M., Campos, T., Geiss, R., Schill, G. P., Fischer, E. V., Kreidenweis, S. M., and DeMott, P. J.: Observations of Ice Nucleating Particles in the Free Troposphere From Western US Wildfires, J. Geophys. Res.-Atmos., 126, e2020JD033752, https://doi.org/10.1029/2020JD033752, 2021.

Bond, T. C. and Bergstrom, R. W.: Light Absorption by Carbonaceous Particles: An Investigative Review, Aerosol Sci. Technol., 40, 27–67, https://doi.org/10.1080/02786820500421521, 2006.

Bond, T. C., Doherty, S. J., Fahey, D. W., Forster, P. M., Berntsen, T., DeAngelo, B. J., Flanner, M. G., Ghan, S., Kaercher, B., Koch, D., Kinne, S., Kondo, Y., Quinn, P. K., Sarofim, M. C., Schultz, M. G., Schulz, M., Venkataraman, C., Zhang, H., Zhang, S., Bellouin, N., Guttikunda, S. K., Hopke, P. K., Jacobson, M. Z., Kaiser, J. W., Klimont, Z., Lohmann, U., Schwarz, J. P., Shindell, D., Storelvmo, T., Warren, S. G., and Zender, C. S.: Bounding the role of black carbon in the climate system: A scientific assessment, J. Geophys. Res.-Atmos., 118, 5380–5552, https://doi.org/10.1002/jgrd.50171, 2013.

Brands, M., Kamphus, M., Böttger, T., Schneider, J., Drewnick, F., Roth, A., Curtius, J., Voigt, C., Borbon, A., Beekmann, M., Bourdon, A., Perrin, T., and Borrmann, S.: Characterization of a Newly Developed Aircraft-Based Laser Ablation Aerosol Mass Spectrometer (ALABAMA) and First Field Deployment in Urban Pollution Plumes over Paris During MEGAPOLI 2009, Aerosol Sci. Technol., 45, 46–64, https://doi.org/10.1080/02786826.2010.517813, 2011.

Brown, R. A., Kercher, A. K., Nguyen, T. H., Nagle, D. C., and Ball, W. P.: Production and characterization of synthetic wood chars for use as surrogates for natural sorbents, Org. Geochem., 37, 321–333, https://doi.org/10.1016/j.orggeochem.2005.10.008, 2006.

Brunauer, S., Emmett, P. H., and Teller, E.: Adsorption of gases in multimolecular layers, J. Am. Chem. Soc., 60, 309–319, https://doi.org/10.1021/ja01269a023, 1938.

Chen, J., Li, C., Ristovski, Z., Milic, A., Gu, Y., Islam, M. S., Wang, S., Hao, J., Zhang, H., He, C., Guo, H., Fu, H., Miljevic, B., Morawska, L., Thai, P., Lam, Y. F., Pereira, G., Ding, A., Huang, X., and Dumka, U. C.: A review of biomass burning: Emissions and impacts on air quality, health and climate in China, Sci. Total Environ., 579, 1000–1034, https://doi.org/10.1016/j.scitotenv.2016.11.025, 2017.

Chou, C., Kanji, Z. A., Stetzer, O., Tritscher, T., Chirico, R., Heringa, M. F., Weingartner, E., Prévôt, A. S. H., Baltensperger, U., and Lohmann, U.: Effect of photochemical ageing on the ice nucleation properties of diesel and wood burning particles, Atmos. Chem. Phys., 13, 761–772, https://doi.org/10.5194/acp-13-761-2013, 2013.

Christenson, H. K.: Two-step crystal nucleation via capillary condensation, Crystengcomm, 15, 2030–2039, https://doi.org/10.1039/c3ce26887j, 2013.

Chylek, P. and Wong, J.: Effect of absorbing aerosols on global radiation budget, Geophys. Res. Lett., 22, 929–931, https://doi.org/10.1029/95GL00800, 1995.

Chylek, P., Jennings, S. G., and Pinnick, R.: AEROSOLS | Soot, in: Encyclopedia of Atmospheric Sciences (Second Edition), edited by: North, G. R., Pyle, J., and Zhang, F., Academic Press, Oxford, 86–91, https://doi.org/10.1016/B978-0-12-382225-3.00375-3, 2015.

Clark, J. S.: Particle Motion and the Theory of Charcoal Analysis: Source Area, Transport, Deposition, and Sampling, Quat. Res., 30, 67–80, https://doi.org/10.1016/0033-5894(88)90088-9, 1988.

Clark, J. S. and Hussey, T. C.: Estimating the mass flux of charcoal from sedimentary records: effects of particle size, morphology, and orientation, Holocene, 6, 129–144, https://doi.org/10.1177/095968369600600201, 1996.

Cofer, W. R., Koutzenogii, K. P., Kokorin, A., and Ezcurra, A.: Biomass Burning Emissions and the Atmosphere, in: Sediment Records of Biomass Burning and Global Change, Berlin, Heidelberg, 189–206, https://doi.org/10.1007/978-3-642-59171-6_9, 1997.

Conedera, M., Manetti, M. C., Giudici, F., and Amorini, E.: Distribution and economic potential of the Sweet chestnut (Castanea sativa Mill.) in Europe, Ecol. Mediterr., 30, 179–193, https://doi.org/10.3406/ecmed.2004.1458, 2004.

Creamean, J. M., Suski, K. J., Rosenfeld, D., Cazorla, A., DeMott, P. J., Sullivan, R. C., White, A. B., Ralph, F. M., Minnis, P., Comstock, J. M., Tomlinson, J. M., and Prather, K. A.: Dust and Biological Aerosols from the Sahara and Asia Influence Precipitation in the Western U.S., Science, 339, 1572–1578, https://doi.org/10.1126/science.1227279, 2013.

Crutzen, P. J. and Andreae, M. O.: Biomass Burning in the Tropics: Impact on Atmospheric Chemistry and Biogeochemical Cycles, Science, 250, 1669–1678, https://doi.org/10.1126/science.250.4988.1669, 1990.

Currie, H. A. and Perry, C. C.: Silica in Plants: Biological, Biochemical and Chemical Studies, Ann. Bot., 100, 1383–1389, https://doi.org/10.1093/aob/mcm247, 2007.

David, R. O., Marcolli, C., Fahrni, J., Qiu, Y. Q., Sirkin, Y. A. P., Molinero, V., Mahrt, F., Bruhwiler, D., Lohmann, U., and Kanji, Z. A.: Pore condensation and freezing is responsible for ice formation below water saturation for porous particles, P. Natl. Acad. Sci. USA, 116, 8184–8189, https://doi.org/10.1073/pnas.1813647116, 2019.

David, R. O., Fahrni, J., Marcolli, C., Mahrt, F., Brühwiler, D., and Kanji, Z. A.: The role of contact angle and pore width on pore condensation and freezing, Atmos. Chem. Phys., 20, 9419–9440, https://doi.org/10.5194/acp-20-9419-2020, 2020.

Demirbas, A.: Effect of Temperature on Pyrolysis Products from Biomass, Energy Sources Part Recovery Util. Environ. Eff., 29, 329–336, https://doi.org/10.1080/009083190965794, 2007.

Demirbas, A. and Arin, G.: An overview of biomass pyrolysis, Energ. Sources, 24, 471–482, https://doi.org/10.1080/00908310252889979, 2002.

DeMott, P. J., Petters, M. D., Prenni, A. J., Carrico, C. M., Kreidenweis, S. M., Collett, J. L., and Moosmuller, H.: Ice nucleation behavior of biomass combustion particles at cirrus temperatures, J. Geophys. Res.-Atmos., 114, D16205, https://doi.org/10.1029/2009jd012036, 2009.

DeMott, P. J., Prenni, A. J., McMeeking, G. R., Sullivan, R. C., Petters, M. D., Tobo, Y., Niemand, M., Möhler, O., Snider, J. R., Wang, Z., and Kreidenweis, S. M.: Integrating laboratory and field data to quantify the immersion freezing ice nucleation activity of mineral dust particles, Atmos. Chem. Phys., 15, 393–409, https://doi.org/10.5194/acp-15-393-2015, 2015.

Ditas, J., Ma, N., Zhang, Y., Assmann, D., Neumaier, M., Riede, H., Karu, E., Williams, J., Scharffe, D., Wang, Q., Saturno, J., Schwarz, J. P., Katich, J. M., McMeeking, G. R., Zahn, A., Hermann, M., Brenninkmeijer, C. A. M., Andreae, M. O., Pöschl, U., Su, H., and Cheng, Y.: Strong impact of wildfires on the abundance and aging of black carbon in the lowermost stratosphere, P. Natl. Acad. Sci. USA, https://doi.org/10.1073/pnas.1806868115, 2018.

Donovan, V. M., Wonkka, C. L., and Twidwell, D.: Surging wildfire activity in a grassland biome, Geophys. Res. Lett., 44, 5986–5993, https://doi.org/10.1002/2017GL072901, 2017.

Earle, M. E., Kuhn, T., Khalizov, A. F., and Sloan, J. J.: Volume nucleation rates for homogeneous freezing in supercooled water microdroplets: results from a combined experimental and modelling approach, Atmos. Chem. Phys., 10, 7945–7961, https://doi.org/10.5194/acp-10-7945-2010, 2010.

Erdmann, N., Dell'Acqua, A., Cavalli, P., Grüning, C., Omenetto, N., Putaud, J.-P., Raes, F., and Dingenen, R. V.: Instrument Characterization and First Application of the Single Particle Analysis and Sizing System (SPASS) for Atmospheric Aerosols, Aerosol Sci. Technol., 39, 377–393, https://doi.org/10.1080/027868290935696, 2005.

Fisher, L. R., Gamble, R. A., and Middlehurst, J.: The Kelvin equation and the capillary condensation of water, Nature, 290, 575–576, https://doi.org/10.1038/290575a0, 1981.

Ford, B., Martin, M. V., Zelasky, S. E., Fischer, E. V., Anenberg, S. C., Heald, C. L., and Pierce, J. R.: Future Fire Impacts on Smoke Concentrations, Visibility, and Health in the Contiguous United States, GeoHealth, 2, 229–247, https://doi.org/10.1029/2018GH000144, 2018.

Fukuta, N.: Activation of Atmospheric Particles as Ice Nuclei in Cold and Dry Air, J. Atmospheric Sci., 23, 741–750, https://doi.org/10.1175/1520-0469(1966)023<0741:aoapai>2.0.co;2, 1966.

Gallavardin, S., Lohmann, U., and Cziczo, D.: Analysis and differentiation of mineral dust by single particle laser mass spectrometry, Int. J. Mass Spectrom., 274, 56–63, https://doi.org/10.1016/j.ijms.2008.04.031, 2008.

Gao, K., Friebel, F., Zhou, C.-W., and Kanji, Z. A.: Enhanced soot particle ice nucleation ability induced by aggregate compaction and densification, Atmos. Chem. Phys., 22, 4985–5016, https://doi.org/10.5194/acp-22-4985-2022, 2022a.

Gao, K., Koch, H.-C., Zhou, C.-W., and Kanji, Z. A.: The dependence of soot particle ice nucleation ability on its volatile content, Environ. Sci. Process. Impacts, 24, 2043–2069, https://doi.org/10.1039/D2EM00158F, 2022b.

Gao, X., Rahim, M. U., Chen, X., and Wu, H.: Significant contribution of organically-bound Mg, Ca, and Fe to inorganic PM_{10} emission during the combustion of pulverized Victorian brown coal, Fuel, 117, 825–832, https://doi.org/10.1016/j.fuel.2013.09.056, 2014.

Gard, E., Mayer, J. E., Morrical, B. D., Dienes, T., Fergenson, D. P., and Prather, K. A.: Real-time analysis of individual atmospheric aerosol particles: Design and performance of a portable ATOFMS, Anal. Chem., 69, 4083–4091, https://doi.org/10.1021/ac970540n, 1997.

Garimella, S., Rothenberg, D. A., Wolf, M. J., David, R. O., Kanji, Z. A., Wang, C., Rösch, M., and Cziczo, D. J.: Uncertainty in counting ice nucleating particles with continuous flow diffusion chambers, Atmos. Chem. Phys., 17, 10855–10864, https://doi.org/10.5194/acp-17-10855-2017, 2017.

Ge, Z., Wexler, A. S., and Johnston, M. V.: Laser Desorption/Ionization of Single Ultrafine Multicomponent Aerosols, Environ. Sci. Technol., 32, 3218–3223, https://doi.org/10.1021/es980104y, 1998.

Gilgen, A., Adolf, C., Brugger, S. O., Ickes, L., Schwikowski, M., van Leeuwen, J. F. N., Tinner, W., and Lohmann, U.: Implementing microscopic charcoal particles into a global aerosol–climate model, Atmos. Chem. Phys., 18, 11813–11829, https://doi.org/10.5194/acp-18-11813-2018, 2018.

Glassman, I., Yetter, R. A., and Glumac, N. G.: Combustion, 5th edn., Elsevier, Amsterdam, ISBN 978-0-12-407913-7 0-12-407913-X, 978-0-12-411555-2 0-12-411555-1, 2014.

Grawe, S., Augustin-Bauditz, S., Hartmann, S., Hellner, L., Pettersson, J. B. C., Prager, A., Stratmann, F., and Wex, H.: The immersion freezing behavior of ash particles from wood and brown coal burning, Atmos. Chem. Phys., 16, 13911–13928, https://doi.org/10.5194/acp-16-13911-2016, 2016.

Grawe, S., Augustin-Bauditz, S., Clemen, H.-C., Ebert, M., Eriksen Hammer, S., Lubitz, J., Reicher, N., Rudich, Y., Schneider, J., Staacke, R., Stratmann, F., Welti, A., and Wex, H.: Coal fly ash: linking immersion freezing behavior and physicochemical particle properties, Atmos. Chem. Phys., 18, 13903–13923, https://doi.org/10.5194/acp-18-13903-2018, 2018.

Gross, D. S., Galli, M. E., Silva, P. J., and Prather, K. A.: Relative sensitivity factors for alkali metal and ammonium cations in single particle aerosol time-of-flight mass spectra, Anal. Chem., 72, 416–422, https://doi.org/10.1021/ac990434g, 2000.

Hammes, K., Smernik, R. J., Skjemstad, J. O., Herzog, A., Vogt, U. F., and Schmidt, M. W. I.: Synthesis and characterisation of laboratory-charred grass straw (*Oryza sativa*) and chestnut wood (*Castanea sativa*) as reference materials for black carbon quantification, Org. Geochem., 37, 1629–1633, https://doi.org/10.1016/j.orggeochem.2006.07.003, 2006.

Hammes, K., Schmidt, M. W. I., Smernik, R. J., Currie, L. A., Ball, W. P., Nguyen, T. H., Louchouarn, P., Houel, S., Gustafsson, Ö., Elmquist, M., Cornelissen, G., Skjemstad, J. O., Masiello, C. A., Song, J., Peng, P., Mitra, S., Dunn, J. C., Hatcher, P. G., Hockaday, W. C., Smith, D. M., Hartkopf-Fröder, C., Böhmer, A., Lüer, B., Huebert, B. J., Amelung, W., Brodowski, S., Huang, L., Zhang, W., Gschwend, P. M., Flores-Cervantes, D. X., Largeau, C., Rouzaud, J.-N., Rumpel, C., Guggenberger, G., Kaiser, K., Rodionov, A., Gonzalez-Vila, F. J., Gonzalez-Perez, J. A., de la Rosa, J. M., Manning, D. A. C., López-Capél, E., and Ding, L.: Comparison of quantification methods to measure fire-derived (black/elemental) carbon in soils and sediments using reference materials from soil, water, sediment and the atmosphere, Glob. Biogeochem. Cycles, 21, GB3016, https://doi.org/10.1029/2006GB002914, 2007.

Hammes, K., Smernik, R. J., Skjemstad, J. O., and Schmidt, M. W. I.: Characterisation and evaluation of reference materials for black carbon analysis using elemental composition, colour, BET surface area and ^{13}C NMR spectroscopy, Appl. Geochem., 23, 2113–2122, https://doi.org/10.1016/j.apgeochem.2008.04.023, 2008.

Han, Y. M., Cao, J. J., Lee, S. C., Ho, K. F., and An, Z. S.: Different characteristics of char and soot in the atmosphere and their ratio as an indicator for source identification in Xi'an, China, Atmos. Chem. Phys., 10, 595–607, https://doi.org/10.5194/acp-10-595-2010, 2010.

Higuchi, K. and Fukuta, N.: Ice in capillaries of solid particles and its effect on their nucleating ability, J. Atmos. Sci., 23, 187–190, https://doi.org/10.1175/1520-0469(1966)023<0187:iitcos>2.0.co;2, 1966.

Hiranuma, N., Augustin-Bauditz, S., Bingemer, H., Budke, C., Curtius, J., Danielczok, A., Diehl, K., Dreischmeier, K., Ebert, M., Frank, F., Hoffmann, N., Kandler, K., Kiselev, A., Koop, T., Leisner, T., Möhler, O., Nillius, B., Peckhaus, A., Rose, D., Weinbruch, S., Wex, H., Boose, Y., DeMott, P. J., Hader, J. D., Hill, T. C. J., Kanji, Z. A., Kulkarni, G., Levin, E. J. T., McCluskey, C. S., Murakami, M., Murray, B. J., Niedermeier, D., Petters, M. D., O'Sullivan, D., Saito, A., Schill, G. P., Tajiri, T., Tolbert, M. A., Welti, A., Whale, T. F., Wright, T. P., and Yamashita, K.: A comprehensive laboratory study on the immersion freezing behavior of illite NX particles: a comparison of 17 ice nucleation measurement techniques, Atmos. Chem. Phys., 15, 2489–2518, https://doi.org/10.5194/acp-15-2489-2015, 2015.

Holden, Z. A., Swanson, A., Luce, C. H., Jolly, W. M., Maneta, M., Oyler, J. W., Warren, D. A., Parsons, R., and Affleck, D.: Decreasing fire season precipitation increased recent western US forest wildfire activity, P. Natl. Acad. Sci., 115, E8349–E8357, https://doi.org/10.1073/pnas.1802316115, 2018.

Hoyle, C. R., Pinti, V., Welti, A., Zobrist, B., Marcolli, C., Luo, B., Höskuldsson, Á., Mattsson, H. B., Stetzer, O., Thorsteinsson, T., Larsen, G., and Peter, T.: Ice nucleation properties of volcanic ash from Eyjafjallajökull, Atmos. Chem. Phys., 11, 9911–9926, https://doi.org/10.5194/acp-11-9911-2011, 2011.

Jahl, L. G., Brubaker, T. A., Polen, M. J., Jahn, L. G., Cain, K. P., Bowers, B. B., Fahy, W. D., Graves, S., and Sullivan, R. C.: Atmospheric aging enhances the ice nucleation ability of biomass-burning aerosol, Sci. Adv., 7, eabd3440, https://doi.org/10.1126/sciadv.abd3440, 2021.

Jahn, L. G., Polen, M. J., Jahl, L. G., Brubaker, T. A., Somers, J., and Sullivan, R. C.: Biomass combustion produces ice-active minerals in biomass-burning aerosol and bottom ash, P. Natl. Acad. Sci., 117, 21928–21937, https://doi.org/10.1073/pnas.1922128117, 2020.

Jantsch, E. and Koop, T.: Cloud Activation via Formation of Water and Ice on Various Types of Porous

Aerosol Particles, ACS Earth Space Chem., 5, 604–617, https://doi.org/10.1021/acsearthspacechem.0c00330, 2021.

Kane, D. B. and Johnston, M. V.: Size and Composition Biases on the Detection of Individual Ultrafine Particles by Aerosol Mass Spectrometry, Environ. Sci. Technol., 34, 4887–4893, https://doi.org/10.1021/es001323y, 2000.

Kanji, Z. A., Welti, A., Chou, C., Stetzer, O., and Lohmann, U.: Laboratory studies of immersion and deposition mode ice nucleation of ozone aged mineral dust particles, Atmos. Chem. Phys., 13, 9097–9118, https://doi.org/10.5194/acp-13-9097-2013, 2013.

Kaufman, Y. J. and Fraser, R. S.: The Effect of Smoke Particles on Clouds and Climate Forcing, Science, 277, 1636–1639, https://doi.org/10.1126/science.277.5332.1636, 1997.

Kaufman, Y. J. and Koren, I.: Smoke and Pollution Aerosol Effect on Cloud Cover, Science, 313, 655–658, https://doi.org/10.1126/science.1126232, 2006.

Kilchhofer, K., Mahrt, F., and Kanji, Z. A.: The Role of Cloud Processing for the Ice Nucleating Ability of Organic Aerosol and Coal Fly Ash Particles, J. Geophys. Res.-Atmos., 126, e2020JD033338, https://doi.org/10.1029/2020JD033338, 2021.

Kim, S., Kramer, R. W., and Hatcher, P. G.: Graphical Method for Analysis of Ultrahigh-Resolution Broadband Mass Spectra of Natural Organic Matter, the Van Krevelen Diagram, Anal. Chem., 75, 5336–5344, https://doi.org/10.1021/ac034415p, 2003.

Koop, T.: Crystals creeping out of cracks, P. Natl. Acad. Sci. USA, 114, 797–799, https://doi.org/10.1073/pnas.1620084114, 2017.

Koop, T., Luo, B., Tsias, A., and Peter, T.: Water activity as the determinant for homogeneous ice nucleation in aqueous solutions, Nature, 406, 611–614, https://doi.org/10.1038/35020537, 2000.

Koren, I., Kaufman, Y. J., Remer, L. A., and Martins, J. V.: Measurement of the Effect of Amazon Smoke on Inhibition of Cloud Formation, Science, 303, 1342–1345, https://doi.org/10.1126/science.1089424, 2004.

Korhonen, K., Kristensen, T. B., Falk, J., Lindgren, R., Andersen, C., Carvalho, R. L., Malmborg, V., Eriksson, A., Boman, C., Pagels, J., Svenningsson, B., Komppula, M., Lehtinen, K. E. J., and Virtanen, A.: Ice-nucleating ability of particulate emissions from solid-biomass-fired cookstoves: an experimental study, Atmos. Chem. Phys., 20, 4951–4968, https://doi.org/10.5194/acp-20-4951-2020, 2020.

Lacher, L., Lohmann, U., Boose, Y., Zipori, A., Herrmann, E., Bukowiecki, N., Steinbacher, M., and Kanji, Z. A.: The Horizontal Ice Nucleation Chamber (HINC): INP measurements at conditions relevant for mixed-phase clouds at the High Altitude Research Station Jungfraujoch, Atmos. Chem. Phys., 17, 15199–15224, https://doi.org/10.5194/acp-17-15199-2017, 2017.

Lehmann, J. and Joseph, S. (Eds.): Biochar for Environmental Management: Science, Technology and Implementation, 2nd edn., Routledge, London, 976 pp., https://doi.org/10.4324/9780203762264, 2015.

Levin, E. J. T., McMeeking, G. R., DeMott, P. J., McCluskey, C. S., Carrico, C. M., Nakao, S., Jayarathne, T., Stone, E. A., Stockwell, C. E., Yokelson, R. J., and Kreidenweis, S. M.: Ice-nucleating particle emissions from biomass combustion and the potential importance of soot aerosol, J. Geophys. Res.-Atmos., 121, 5888–5903, https://doi.org/10.1002/2016JD024879, 2016.

Li, J., Posfai, M., Hobbs, P. V., and Buseck, P. R.: Individual aerosol particles from biomass burning in southern Africa: 2, Compositions and aging of inorganic particles, J. Geophys. Res.-Atmospheres, 108, 8484, https://doi.org/10.1029/2002jd002310, 2003.

Lohmann, U., Lüönd, F., and Mahrt, F.: An Introduction to Clouds: From the Microscale to Climate, 1st edn., Cambridge University Press, Cambridge, https://doi.org/10.1017/CBO9781139087513, 2016.

Lüönd, F., Stetzer, O., Welti, A., and Lohmann, U.: Experimental study on the ice nucleation ability of size-selected kaolinite particles in the immersion mode, J. Geophys. Res.-Atmospheres, 115, D14201, https://doi.org/10.1029/2009jd012959, 2010.

Mahrt, F., Marcolli, C., David, R. O., Grönquist, P., Barthazy Meier, E. J., Lohmann, U., and Kanji, Z. A.: Ice nucleation abilities of soot particles determined with the Horizontal Ice Nucleation Chamber, Atmos. Chem. Phys., 18, 13363–13392, https://doi.org/10.5194/acp-18-13363-2018, 2018.

Mahrt, F., Kilchhofer, K., Marcolli, C., Grönquist, P., David, R. O., Rösch, M., Lohmann, U., and Kanji, Z. A.: The Impact of Cloud Processing on the Ice Nucleation Abilities of Soot Particles at Cirrus Temperatures, J. Geophys. Res.-Atmos., 125, e2019JD030922, https://doi.org/10.1029/2019JD030922, 2020.

Mahrt, F., Rösch, C., Gao, K., Dreimol, C. H., Zawadowicz, M. A., and Kanji, Z. A.: Physicochemical properties of charcoal aerosols derived from biomass pyrolysis affect their ice-nucleating abilities at cirrus and mixed-phase cloud conditions, ETH Zurich [data set], https://doi.org/10.3929/ethz-b-000591583, 2023.

Marcolli, C.: Deposition nucleation viewed as homogeneous or immersion freezing in pores and cavities, Atmos. Chem. Phys., 14, 2071–2104, https://doi.org/10.5194/acp-14-2071-2014, 2014.

Marcolli, C.: Technical note: Fundamental aspects of ice nucleation via pore condensation and freezing including Laplace pressure and growth into macroscopic ice, Atmos. Chem. Phys., 20, 3209–3230, https://doi.org/10.5194/acp-20-3209-2020, 2020.

Marcolli, C., Mahrt, F., and Kärcher, B.: Soot PCF: pore condensation and freezing framework for soot aggregates, Atmos. Chem. Phys., 21, 7791–7843, https://doi.org/10.5194/acp-21-7791-2021, 2021.

Marlon, J. R., Bartlein, P. J., Carcaillet, C., Gavin, D. G., Harrison, S. P., Higuera, P. E., Joos, F., Power, M. J., and Prentice, I. C.: Climate and human influences on global biomass burning over the past two millennia, Nat. Geosci., 1, 697–702, https://doi.org/10.1038/ngeo313, 2008.

Marlon, J. R., Bartlein, P. J., Gavin, D. G., Long, C. J., Anderson, R. S., Briles, C. E., Brown, K. J., Colombaroli, D., Hallett, D. J., Power, M. J., Scharf, E. A., and Walsh, M. K.: Long-term perspective on wildfires in the western USA, P. Natl. Acad. Sci., 109, E535–E543, https://doi.org/10.1073/pnas.1112839109, 2012.

Marsden, N. A., Ullrich, R., Möhler, O., Eriksen Hammer, S., Kandler, K., Cui, Z., Williams, P. I., Flynn, M. J., Liu, D., Allan, J. D., and Coe, H.: Mineralogy and mixing state of north African mineral dust by online single-particle mass spectrometry, Atmos. Chem. Phys., 19, 2259–2281, https://doi.org/10.5194/acp-19-2259-2019, 2019.

Masiello, C. A.: New directions in black carbon organic geochemistry, Mar. Chem., 92, 201–213, https://doi.org/10.1016/j.marchem.2004.06.043, 2004.

Maudlin, L. C., Wang, Z., Jonsson, H. H., and Sorooshian, A.: Impact of wildfires on size-resolved aerosol composition at a coastal California site, Atmos. Environ., 119, 59–68, https://doi.org/10.1016/j.atmosenv.2015.08.039, 2015.

McCluskey, C. S., DeMott, P. J., Prenni, A. J., Levin, E. J. T., McMeeking, G. R., Sullivan, A. P., Hill, T. C. J., Nakao, S., Carrico, C. M., and Kreidenweis, S. M.: Characteristics of atmospheric ice nucleating particles associated with biomass burning in the US: Prescribed burns and wildfires, J. Geophys. Res.-Atmos., 119, 10458–10470, https://doi.org/10.1002/2014JD021980, 2014.

Mondal, N. and Sukumar, R.: Fire and soil temperatures during controlled burns in seasonally dry tropical forests of southern India, Curr. Sci., 107, 1590–1594, 2014.

Moritz, M. A., Parisien, M.-A., Batllori, E., Krawchuk, M. A., Dorn, J. V., Ganz, D. J., and Hayhoe, K.: Climate change and disruptions to global fire activity, Ecosphere, 3, art49, https://doi.org/10.1890/ES11-00345.1, 2012.

Murphy, D. M. and Koop, T.: Review of the vapour pressures of ice and supercooled water for atmospheric applications, Q. J. Roy. Meteor. Soc., 131, 1539–1565, https://doi.org/10.1256/qj.04.94, 2005.

Murray, B. J., O'Sullivan, D., Atkinson, J. D., and Webb, M. E.: Ice nucleation by particles immersed in supercooled cloud droplets, Chem. Soc. Rev., 41, 6519–6554, https://doi.org/10.1039/C2CS35200A, 2012.

Nichman, L., Wolf, M., Davidovits, P., Onasch, T. B., Zhang, Y., Worsnop, D. R., Bhandari, J., Mazzoleni, C., and Cziczo, D. J.: Laboratory study of the heterogeneous ice nucleation on black-carbon-containing aerosol, Atmos. Chem. Phys., 19, 12175–12194, https://doi.org/10.5194/acp-19-12175-2019, 2019.

Noble, C. A. and Prather, K. A.: Real-time measurement of correlated size and composition profiles of individual atmospheric aerosol particles, Environ. Sci. Technol., 30, 2667–2680, https://doi.org/10.1021/es950669j, 1996.

Ouf, F.-X., Bourrous, S., Vallières, C., Yon, J., and Lintis, L.: Specific surface area of combustion emitted particles: Impact of primary particle diameter and organic content, J. Aerosol Sci., 137, 105436, https://doi.org/10.1016/j.jaerosci.2019.105436, 2019.

Pardo, M., Li, C., He, Q., Levin-Zaidman, S., Tsoory, M., Yu, Q., Wang, X., and Rudich, Y.: Mechanisms of lung toxicity induced by biomass burning aerosols, Part. Fibre Toxicol., 17, 4, https://doi.org/10.1186/s12989-020-0337-x, 2020.

Penner, J. E., Dickinson, R. E., and O'Neill, C. A.: Effects of Aerosol from Biomass Burning on the Global Radiation Budget, Science, 256, 1432–1434, https://doi.org/10.1126/science.256.5062.1432, 1992.

Petters, M. D., Parsons, M. T., Prenni, A. J., DeMott, P. J., Kreidenweis, S. M., Carrico, C. M., Sullivan, A. P., McMeeking, G. R., Levin, E., Wold, C. E., Collett, J. L., and Moosmuller, H.: Ice nuclei emissions from biomass burning, J. Geophys. Res.-Atmospheres, 114, D07209, https://doi.org/10.1029/2008jd011532, 2009.

Petzold, A., Ogren, J. A., Fiebig, M., Laj, P., Li, S.-M., Baltensperger, U., Holzer-Popp, T., Kinne, S., Pappalardo, G., Sugimoto, N., Wehrli, C., Wiedensohler, A., and Zhang, X.-Y.: Recommendations for reporting "black carbon" measurements, Atmos. Chem. Phys., 13, 8365–8379, https://doi.org/10.5194/acp-13-8365-2013, 2013.

Popovicheva, O., Persiantseva, N. M., Shonija, N. K., DeMott, P., Koehler, K., Petters, M., Kreidenweis, S., Tishkova, V., Demirdjian, B., and Suzanne, J.: Water interaction with hydrophobic and hydrophilic soot particles, Phys. Chem. Chem. Phys., 10, 2332–2344, https://doi.org/10.1039/B718944N, 2008.

Popovitcheva, O. B., Persiantseva, N. M., Trukhin, M. E., Rulev, G. B., Shonija, N. K., Buriko, Y. Y., Starik, A. M., Demirdjian, B., Ferry, D., and Suzanne, J.: Experimental characterization of aircraft combustor soot: Microstructure, surface area, porosity and water adsorption, Phys. Chem. Chem. Phys., 2, 4421–4426, https://doi.org/10.1039/b004345l, 2000.

Posfai, M., Simonics, R., Li, J., Hobbs, P. V., and Buseck, P. R.: Individual aerosol particles from biomass burning in southern Africa: 1. Compositions and size distributions of carbonaceous particles, J. Geophys. Res.-Atmospheres, 108, 8483, https://doi.org/10.1029/2002jd002291, 2003.

Prather, K. A., Nordmeyer, T., and Salt, K.: Real-Time Characterization of Individual Aerosol-PArticles using Time-of-Flight Mass-Spectrometry, Anal. Chem., 66, 1403–1407, https://doi.org/10.1021/ac00081a007, 1994.

Pratt, K. A., DeMott, P. J., French, J. R., Wang, Z., Westphal, D. L., Heymsfield, A. J., Twohy, C. H., Prenni, A. J., and Prather, K. A.: In situ detection of biological particles in cloud ice-crystals, Nat. Geosci., 2, 397–400, https://doi.org/10.1038/ngeo521, 2009.

Reddington, C. L., Butt, E. W., Ridley, D. A., Artaxo, P., Morgan, W. T., Coe, H., and Spracklen, D. V.: Air quality and human health improvements from reductions in deforestation-related fire in Brazil, Nat. Geosci., 8, 768–771, https://doi.org/10.1038/ngeo2535, 2015.

Reddy, M. S. and Boucher, O.: A study of the global cycle of carbonaceous aerosols in the LMDZT general circulation model, J. Geophys. Res.-Atmos., 109, D14202, https://doi.org/10.1029/2003JD004048, 2004.

Reilly, P. T. A., Lazar, A. C., Gieray, R. A., Whitten, W. B., and Ramsey, J. M.: The Elucidation of Charge-Transfer-Induced Matrix Effects in Environmental Aerosols Via Real-Time Aerosol Mass Spectral Analysis of Individual Airborne Particles, Aerosol Sci. Technol., 33, 135–152, https://doi.org/10.1080/027868200410895, 2000.

Safdari, M.-S., Amini, E., Weise, D. R., and Fletcher, T. H.: Heating rate and temperature effects on pyrolysis products from live wildland fuels, Fuel, 242, 295–304, https://doi.org/10.1016/j.fuel.2019.01.040, 2019.

Sander, P. M. and Gee, C. T.: Fossil charcoal: techniques and applications, Rev. Palaeobot. Palynol., 63, 269–279, https://doi.org/10.1016/0034-6667(90)90104-Q, 1990.

Santín, C., Doerr, S. H., Kane, E. S., Masiello, C. A., Ohlson, M., de la Rosa, J. M., Preston, C. M., and Dittmar, T.: Towards a global assessment of pyrogenic carbon from vegetation fires, Glob. Change Biol., 22, 76–91, https://doi.org/10.1111/gcb.12985, 2016.

Schill, G. P., Froyd, K. D., Bian, H., Kupc, A., Williamson, C., Brock, C. A., Ray, E., Hornbrook, R. S., Hills, A. J., Apel, E. C., Chin, M., Colarco, P. R., and Murphy, D. M.: Widespread biomass burning smoke throughout the remote troposphere, Nat. Geosci., 13, 422–427, https://doi.org/10.1038/s41561-020-0586-1, 2020.

Schmidt, M. W. I.: Charcoal particles, University of Zurich [sample], https://www.geo.uzh.ch/en/units/2b/Services/BC-material/Black-carbon-rich-materials.html, last access: 12 January 2023.

Schmidt, S., Schneider, J., Klimach, T., Mertes, S., Schenk, L. P., Kupiszewski, P., Curtius, J., and Borrmann, S.: Online single particle analysis of ice particle residuals from mountain-top mixed-phase clouds using laboratory derived particle type assignment, Atmos. Chem. Phys., 17, 575–594, https://doi.org/10.5194/acp-17-575-2017, 2017.

Sharma, R. K., Wooten, J. B., Baliga, V. L., Lin, X., Geoffrey Chan, W., and Hajaligol, M. R.: Characterization of chars from pyrolysis of lignin, Fuel, 83, 1469–1482, https://doi.org/10.1016/j.fuel.2003.11.015, 2004.

Sierau, B., Chang, R. Y.-W., Leck, C., Paatero, J., and Lohmann, U.: Single-particle characterization of the high-Arctic summertime aerosol, Atmos. Chem. Phys., 14, 7409–7430, https://doi.org/10.5194/acp-14-7409-2014, 2014.

Sing, K. S. W., Everett, D. H., Haul, R. A. W., Moscou, L., Pierotti, R. A., Rouquerol, J., and Siemieniewska, T.: Reporting physisorption data for gas solid systems with special reference to the determination of surface-area and porosity, Pure Appl. Chem., 57, 603–619, https://doi.org/10.1351/pac198557040603, 1985.

Singh, G., Gupta, M. K., Chaurasiya, S., Sharma, V. S., and Pimenov, D. Y.: Rice straw burning: a review on its global prevalence and the sustainable alternatives for its effective mitigation, Environ. Sci. Pollut. Res., 28, 32125–32155, https://doi.org/10.1007/s11356-021-14163-3, 2021.

Sokolik, I. N., Soja, A. J., DeMott, P. J., and Winker, D.: Progress and Challenges in Quantifying Wildfire Smoke Emissions, Their Properties, Transport, and Atmospheric Impacts, J. Geophys. Res.-Atmos., 124, 13005–13025, https://doi.org/10.1029/2018JD029878, 2019.

Stetzer, O., Baschek, B., Lueoeond, F., and Lohmann, U.: The Zurich Ice Nucleation Chamber (ZINC) – A new instrument to investigate atmospheric ice formation, Aerosol Sci. Technol., 42, 64–74, https://doi.org/10.1080/02786820701787944, 2008.

Stratakis, G. A. and Stamatelos, A. M.: Thermogravimetric analysis of soot emitted by a modern diesel engine run on catalyst-doped fuel, Combust. Flame, 132, 157–169, https://doi.org/10.1016/s0010-2180(02)00432-7, 2003.

Sultana, C. M., Cornwell, G. C., Rodriguez, P., and Prather, K. A.: FATES: a flexible analysis toolkit for the exploration of single-particle mass spectrometer data, Atmos. Meas. Tech., 10, 1323–1334, https://doi.org/10.5194/amt-10-1323-2017, 2017a.

Sultana, C. M., Cornwell, G. C., and Rodriguez, P.: KPratherLab/FATESmatlabToolKit: Version 1 of FATES (v1.0.0), Zenodo [code], https://doi.org/10.5281/zenodo.398847, 2017b.

Thommes, M., Kaneko, K., Neimark, A. V., Olivier, J. P., Rodriguez-Reinoso, F., Rouquerol, J., and Sing, K. S. W.: Physisorption of gases, with special reference to the evaluation of surface area and pore size distribution (IUPAC Technical Report), Pure Appl. Chem., 87, 1051–1069, https://doi.org/10.1515/pac-2014-1117, 2015.

Tinner, W., Hofstetter, S., Zeugin, F., Conedera, M., Wohlgemuth, T., Zimmermann, L., and Zweifel, R.: Long-distance transport of macroscopic charcoal by an intensive crown fire in the Swiss Alps – implications for fire history reconstruction, Holocene, 16, 287–292, https://doi.org/10.1191/0959683606hl925rr, 2006.

Twohy, C. H., DeMott, P. J., Pratt, K. A., Subramanian, R., Kok, G. L., Murphy, S. M., Lersch, T., Heymsfield, A. J., Wang, Z. E., Prather, K. A., and Seinfeld, J. H.: Relationships of Biomass-Burning Aerosols to Ice in Orographic Wave Clouds, J. Atmos. Sci., 67, 2437–2450, https://doi.org/10.1175/2010jas3310.1, 2010.

Umo, N. S., Murray, B. J., Baeza-Romero, M. T., Jones, J. M., Lea-Langton, A. R., Malkin, T. L., O'Sullivan, D., Neve, L., Plane, J. M. C., and Williams, A.: Ice nucleation by combustion ash particles at conditions relevant to mixed-phase clouds, Atmos. Chem. Phys., 15, 5195–5210, https://doi.org/10.5194/acp-15-5195-2015, 2015.

Umo, N. S., Wagner, R., Ullrich, R., Kiselev, A., Saathoff, H., Weidler, P. G., Cziczo, D. J., Leisner, T., and Möhler, O.: Enhanced ice nucleation activity of coal fly ash aerosol particles initiated by ice-filled pores, Atmos. Chem. Phys., 19, 8783–8800, https://doi.org/10.5194/acp-19-8783-2019, 2019.

Vali, G.: Interpretation of freezing nucleation experiments: singular and stochastic; sites and surfaces, Atmos. Chem. Phys., 14, 5271–5294, https://doi.org/10.5194/acp-14-5271-2014, 2014.

Vali, G., DeMott, P. J., Möhler, O., and Whale, T. F.: Technical Note: A proposal for ice nucleation terminology, Atmos. Chem. Phys., 15, 10263–10270, https://doi.org/10.5194/acp-15-10263-2015, 2015.

Vassilev, S. V., Baxter, D., Andersen, L. K., and Vassileva, C. G.: An overview of the chemical composition of biomass, Fuel, 89, 913–933, https://doi.org/10.1016/j.fuel.2009.10.022, 2010.

Vassilev, S. V., Baxter, D., Andersen, L. K., Vassileva, C. G., and Morgan, T. J.: An overview of the organic and inorganic phase composition of biomass, Fuel, 94, 1–33, https://doi.org/10.1016/j.fuel.2011.09.030, 2012.

Vassilev, S. V., Baxter, D., and Vassileva, C. G.: An overview of the behaviour of biomass during combustion: Part I. Phase-mineral transformations of organic and inorganic matter, Fuel, 112, 391–449, https://doi.org/10.1016/j.fuel.2013.05.043, 2013.

Wagner, R., Jähn, M., and Schepanski, K.: Wildfires as a source of airborne mineral dust – revisiting a conceptual model using large-eddy simulation (LES), Atmos. Chem. Phys., 18, 11863–11884, https://doi.org/10.5194/acp-18-11863-2018, 2018.

Welti, A., Lüönd, F., Stetzer, O., and Lohmann, U.: Influence of particle size on the ice nucleating ability of mineral dusts, Atmos. Chem. Phys., 9, 6705–6715, https://doi.org/10.5194/acp-9-6705-2009, 2009.

Welti, A., Lüönd, F., Kanji, Z. A., Stetzer, O., and Lohmann, U.: Time dependence of immersion freezing: an experimental study on size selected kaolinite particles, Atmos. Chem. Phys., 12, 9893–9907, https://doi.org/10.5194/acp-12-9893-2012, 2012.

Welti, A., Kanji, Z. A., Lüönd, F., Stetzer, O., and Lohmann, U.: Exploring the Mechanisms of Ice Nucleation on Kaolinite: From Deposition Nucleation to Condensation Freezing, J. Atmospheric Sci., 71, 16–36, https://doi.org/10.1175/jas-d-12-0252.1, 2014.

van der Werf, G. R., Randerson, J. T., Giglio, L., Collatz, G. J., Mu, M., Kasibhatla, P. S., Morton, D. C., DeFries, R. S., Jin, Y., and van Leeuwen, T. T.: Global fire emissions and the contribution of deforestation, savanna, forest, agricultural, and peat fires (1997–2009), Atmos. Chem. Phys., 10, 11707–11735, https://doi.org/10.5194/acp-10-11707-2010, 2010.

Westerling, A. L., Hidalgo, H. G., Cayan, D. R., and Swetnam, T. W.: Warming and Earlier Spring Increase Western U.S. Forest Wildfire Activity, Science, 313, 940–943, https://doi.org/10.1126/science.1128834, 2006.

Wiedensohler, A.: An approximation of the bipolar charge-distribution for particles in the sub-micron size range, J. Aerosol Sci., 19, 387–389, https://doi.org/10.1016/0021-8502(88)90278-9, 1988.

Williams, P. T. and Besler, S.: The influence of temperature and heating rate on the slow pyrolysis of biomass, Renew. Energy, 7, 233–250, https://doi.org/10.1016/0960-1481(96)00006-7, 1996.

Xu, J., Wang, H., Li, X., Li, Y., Wen, J., Zhang, J., Shi, X., Li, M., Wang, W., Shi, G., and Feng, Y.: Refined source apportionment of coal combustion sources by using single particle mass spectrometry, Sci. Total Environ., 627, 633–646, https://doi.org/10.1016/j.scitotenv.2018.01.269, 2018.

Yue, S., Zhu, J., Chen, S., Xie, Q., Li, W., Li, L., Ren, H., Su, S., Li, P., Ma, H., Fan, Y., Cheng, B., Wu, L., Deng, J., Hu, W., Ren, L., Wei, L., Zhao, W., Tian, Y., Pan, X., Sun, Y., Wang, Z., Wu, F., Liu, C.-Q., Su, H., Penner, J. E., Pöschl, U., Andreae, M. O., Cheng, Y., and Fu, P.: Brown carbon from biomass burning imposes strong circum-Arctic warming, One Earth, 5, 293–304, https://doi.org/10.1016/j.oneear.2022.02.006, 2022.

Zawadowicz, M. A., Froyd, K. D., Murphy, D. M., and Cziczo, D. J.: Improved identification of primary biological aerosol particles using single-particle mass spectrometry, Atmos. Chem. Phys., 17, 7193–7212, https://doi.org/10.5194/acp-17-7193-2017, 2017.

Zelenyuk, A. and Imre, D.: Single particle laser ablation time-of-flight mass spectrometer: An introduction to SPLAT, Aerosol Sci. Technol., 39, 554–568, https://doi.org/10.1080/027868291009242, 2005.

Zhang, C., Zhang, Y., Wolf, M. J., Nichman, L., Shen, C., Onasch, T. B., Chen, L., and Cziczo, D. J.: The effects of morphology, mobility size, and secondary organic aerosol (SOA) material coating on the ice nucleation activity of black carbon in the cirrus regime, Atmos. Chem. Phys., 20, 13957–13984, https://doi.org/10.5194/acp-20-13957-2020, 2020.

Zimmerman, A. R. and Mitra, S.: Trial by Fire: On the Terminology and Methods Used in Pyrogenic Organic Carbon Research, Front. Earth Sci., 5, 95, https://doi.org/10.3389/feart.2017.00095, 2017.